ETH
Eidgenössische Technische Hochschule Zürich
Swiss Federal Institute of Technology Zurich

Coupled Lumped-element Resonators with Periodic Boundary Conditions

Semester Thesis

Arno Bargerbos

October 16th, 2015

Supervisor: MSc. Michele Collodo

Group leader: Prof. Andreas Wallraff

Group: Quantum Device Lab, ETH Zürich

Abstract

In this thesis we investigate the scattering matrix elements of systems of coupled lumped element resonators with periodic boundary conditions. Following previous work on linear arrays of such resonators [1], we aim to extract how the relevant parameters depend on the fabrication of the circuits by studying how they vary in different samples. As the previously researched systems did not have periodicity, both the theory and analysis methods have to be adapted. Through the input output formalism and analysis of the system's Hamiltonian we study types of symmetries exhibited by the circuit, and their effect on its scattering matrix elements. We then perform dipstick measurements of a wide variety of circular circuits with different fabrication parameters and geometries to obtain these matrix elements, which we fit to the theoretical model, allowing us to extract dependencies. All together the research aims to fully understand the system and the fabricational dependence of its parameters in order to eventually explore more exotic physics, for example through the introduction of non linear elements.

Acknowledgements

I would like to thank MSc. Michele Collodo, my supervisor from the Quantum Device Lab at the Swiss Federal Institute of Technology in Zürich (ETHZ) where I performed my experiments. He has provided we with many hours of valuable explanations and feedback, and has helped me gain a deep understanding of the theory of lumped element resonators as well as the experimental procedures involved with dipsticks and vector network analysers. Moreover, I would also like to thank Prof. Andreas Wallraff, the group leader of the Quantum Device lab. By allowing me to work in this group I was given the unique opportunity to work in a top-notch experimental physics environment alongside experienced researchers. I would also like to thank Dr. Anton Potočnik, who has also given me valuable feedback at all stages of the project.

Contents

Contents **iii**

1 Introduction **1**

2 Theory **3**
2.1 Lumped-element Resonators 3
2.2 Hamiltonian in Second Quantization 5
2.3 Input-output Theory 6
2.4 Degeneracies and Dark Modes 7
2.4.1 Eigenvector Analysis 9
2.4.2 Dispersion Relation 13

3 Experimental Setup **18**
3.1 Devices Studied 18
3.1.1 Components of the Devices 18
3.1.2 Geometries and Fabrication Variations 19
3.2 Dipstick Measurements 20
3.3 Fitting the Data 22

4 Results and Discussion **27**
4.1 Circular Quatromer 27
4.1.1 CQJ 27
4.1.2 CQC 29
4.1.3 CQK 31
4.1.4 CQL 33
4.1.5 Comparison of the circuits 33
4.2 Circular Trimer 35
4.3 Circular Hexamer 37
4.4 Circular Octomer 37

5 Conclusion and Outlook **40**

A Visualizing Eigenvectors of Systems with Periodic Boundary Conditions **44**

Bibliography **51**

Chapter 1

Introduction

In the past century scientists have uncovered the exotic features of quantum mechanics; laws of physics describing the world at the small scale. A rich theory with counter-intuitive aspects such as quantum measurements and entanglement, it has changed our most fundamental understanding of nature and led to numerous new areas of research. A well known example of this is the field of quantum information science, which investigates how such quantum mechanical phenomena can be used to gain an advantage over technology relying solely on classical principles. [2]

One of such areas that has seen a lot of interest in recent years is quantum simulation, which aims to understand quantum systems that prove to be complicated to study on their own and are intractable for even the most powerful supercomputers built to date. Typically one of two approaches is taken; digital or analog simulation. A digital quantum simulator would act akin to a modern classical computer, executing a series of universal gates in order to fully reproduce the (Hamiltonian driven) unitary evolution of the quantum system to be studied. [3] An analog quantum simulator shows more similarity to how one would use a wind tunnel to investigate the drag and lift of an air plane wing. Rather than using gates to artificially produce the unitary evolution from the bottom up, one uses a different quantum system that mimics the system of interest through emulation. [3] For this to be possible the Hamiltonian of the system to be simulated is mapped directly onto the Hamiltonian of the simulator, which ideally can be controlled to some extent. As the mimicking might not be exact, the simulator may only partly reproduce the dynamics of the system. This however does not have to be problematic. Even without being able to reproduce the full quantitative details, analogue simulators can still provide valuable qualitative answers, for example about whether a set of physical conditions leads to a phase transition in a certain system. [3]

One such phenomena for which analog simulation could provide qualita-

tive answers is photosynthesis. Whereas biology is typically considered to operate in the classical physics regime, it is observed that the photosynthetic light-harvesting apparatus exhibits an unusually high efficiency in moving energy from absorbed photons to the reaction center that could potentially be explained by long-lived quantum coherences. [4, 5] This is peculiar as in typical biological systems, coherences between states decay much faster than the states themselves can relax. This implies that the coherences cannot influence the relaxation process itself, which does not appear to be the case for photosynthesis. [4] Studying how these apparent long lived coherences come about in the organic systems themselves has proven difficult as the contributing organic compounds complex. By constructing a quantum system analogous to the light-harvesting apparatus one can hope to gain more insight into these phenomena in a more tractable system.

Systems that would lend themselves well to the specific physical and geometric requirements [6] of the problem are coupled non-linear cavities. A well studied way of constructing such a system is through lumped element resonators, electronic circuits containing elements such as capacitances and Josephson junctions. [1] However, before one can hope to use such a system to study these intricate and exotic physical phenomena, precise understanding and control of the various parameters is required. To do so this thesis studies a simplified version of such a system, being a circuit of coupled linear resonators with periodic boundary conditions. These systems can be readily described by simple electronic circuit theory, the physics of which is accurately governed by circuit quantum electrodynamics. The predictions from theory can then be matched to actual measurements, and in turn the various parameters controlled by fabrication can be quantified, providing the researchers with great control over the Hamiltonian of the system.

A similar study of such parameter dependencies was previously performed for a linear array of coupled lumped element resonators [1], in which accurate relationships were found between fabrication and measurement. In this thesis we follow a similar approach: by analyzing the circuit through the second quantization and input-output theory frameworks, we attempt to find a model for the physics of the system. We then employ dipstick measurements performed at liquid helium temperatures to extract scattering matrix elements, which are subsequently fit to the derived model. From this we aim to subtract the Hamiltonian's parameter dependencies on fabrication parameters, giving insight and control of the system and paving the way to controlling more complicated systems.

Chapter 2

Theory

In this chapter we discuss a theoretical framework that encompasses the physics probed in the performed experiments. We first establish a basic description of the system being studied. We then use the Lagrange, Hamilton and second quantization formalisms to quantify the physical properties of the system. This in turn allows us to apply input output theory in order to consider how to characterize the system through measurement. Finally, we discuss some of the physical intricacies arising from the chosen geometry from the perspective of eigenvalues, eigenvectors and dispersion relations.

2.1 Lumped-element Resonators

In this thesis we study various instances of coupled lumped-element resonators with periodic boundary conditions. Chapter 3 covers some of the physical considerations of realising and describing these systems, but here we simply reduce them to their circuit representation. Doing so allows one to model the system as a series of RLC parallel circuits, an often encountered and well studied structure [7]. Each circuit consist of three components: the resistor R, the inductor L and the capacitor C. The capacitor and inductor periodically release and absorb energy, while the resistor dissipates energy; an RLC circuit is thus a (damped) harmonic oscillator, which has a characteristic frequency of oscillation ω_0.

In general our system consists of N such RLC circuits, labelled i, which individually consist of the aforementioned three components: a capacitor C_i, an inductor L_i, a resistor R_i, and thus their individual resonance frequency ω_i. These circuits are then coupled through N capacitors connecting them, much like N mass-spring systems connected to each other via more springs. Labelled C_{Ji}, each of the capacitors connects circuits i and $i+1$. The final coupling capacitor C_{JN} connects circuit N and 1; this establishes the periodic boundary condition of our system. In order to probe the system, we

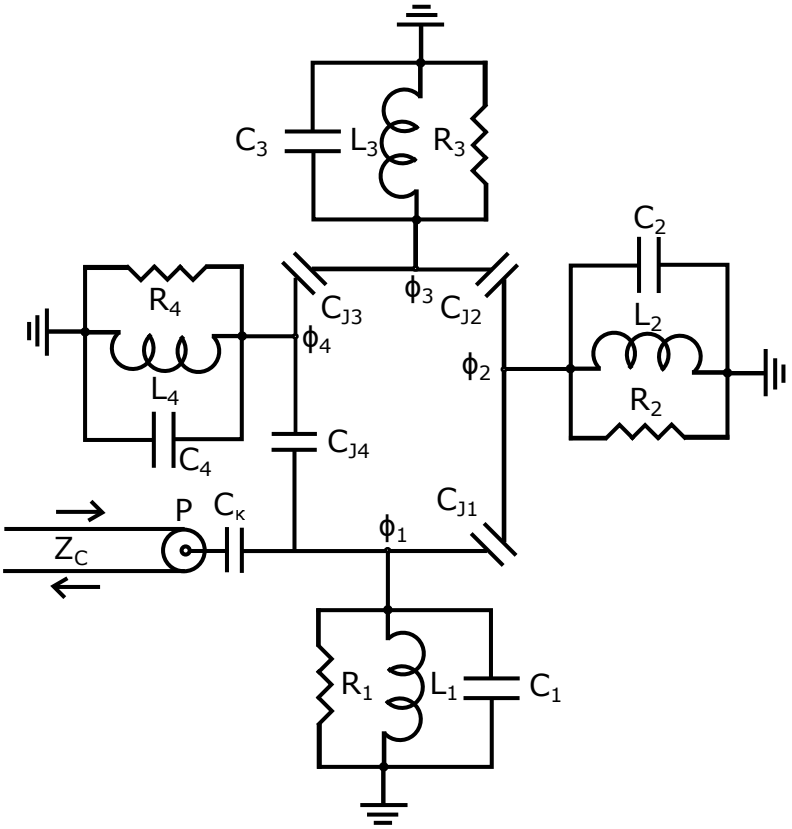

Figure 2.1: The circuit representation of the circular quatromer (CQ). It consists of a series of 4 parallel RLC circuits with capacitance C_i, inductance L_i and resistance R_i. They are coupled to each other via coupling capacitances C_{Ji}, and in this illustration RLC circuit 1 is coupled to an external transmission line P (with characteristic impedance Z_C) via coupling capacitance C_κ. The arrows schematically indicate the direction of current flowing into and out of the system. The flux nodes are denoted by ϕ_i.

connect it to an external entity. To do so, one or more of the RLC circuits is coupled to the environment via an extra coupling capacitor $C_{\kappa i}$, which connects the system to a transmission line P_i (with characteristic impedance Z_{Ci}). In the case of a single instance of external coupling the subscript i is dropped for these three parameters. Electric signals can enter and leave the circuit through this coupling, and the harmonic oscillators are therefore not only damped but also driven. Figure 2.1 illustrates this system for $N = 4$ resonators; a system we call the circular quatromer (CQ).

2.2 Hamiltonian in Second Quantization

The physics of a single RLC circuit is readily described using the Lagrange, Hamilton and second quantization formalisms [1], which together provide insight into the system's properties in the quantum regime. Here we will employ these same techniques and derive the Hamiltonian of our system in the second quantization framework. However, we will begin doing so ignoring any coupling to the environment, as well as the internal losses. These factors are instead taken into account in section 2.3 using input output theory. A pictorial way of doing so would be removing the resistances R_i, the coupling capacitance C_κ and transmission line P in Figure 2.1.

We begin by defining the Lagrangian of our system of N coupled parallel LC circuits, using the flux nodes ϕ_i (defined through $V_i = \dot{\phi}_i$) as coordinates [1]

$$\mathcal{L} = \frac{1}{2}\sum_{i=1}^{N} C_i \dot{\phi}_i^2 - \frac{1}{2}\sum_{i=1}^{N} \frac{\phi_i^2}{L_i} + \frac{1}{2}\sum_{i=1}^{N} C_{Ji}\left(\dot{\phi}_{i+1} - \dot{\phi}_i\right)^2 \tag{2.1}$$

where one has to apply the periodic boundary condition

$$\dot{\phi}_{N+1} = \dot{\phi}_1 \tag{2.2}$$

The above can be written in matrix form as

$$\mathcal{L} = \frac{1}{2}\dot{\Phi}^T \underline{C} \dot{\Phi} - \frac{1}{2}\Phi^T \underline{L}^{-1} \Phi \tag{2.3}$$

with $\Phi = (\phi_1, \phi_2, ..., \phi_N)$ a vector of flux nodes, $\underline{L}$ a diagonal matrix of inductances, and $\underline{C}$ the sum of a tridiagonal matrix and a matrix of two extremal off diagonal values, both consisting of capacitances. Here the tridiagonal matrix comes from the coupling between adjacent resonators in the absence of periodic boundary conditions, while the extremal off diagonal add exactly these boundary terms. We can now employ the definition of the canonical conjugate momentum $q_i \equiv \frac{\partial \mathcal{L}}{\partial \dot{\phi}_i} = C_{ij}\dot{\phi}_j$ to obtain the Hamiltonian in matrix form

$$\mathcal{H} = \frac{1}{2} Q^T \underline{C}^{-1} Q + \frac{1}{2}\Phi^T \underline{L}^{-1} \Phi \tag{2.4}$$

where we define Q in similar fashion to Φ; as the vector $Q = (q_1, q_2, ..., q_N)$, which is a vector of charges. We then elevate our coordinates to operators through the enforcement of the canonical commutation relation $\left[\hat{q}_i, \hat{\phi}_j\right] = -i\hbar\delta_{ij}$. This allows us to define creation and annihilation operators $\hat{a}_i^\dagger, \hat{a}_i$, which when combined with the rotating wave approximation leave the Hamiltonian in our desired form

$$\mathcal{H} = \sum_{i=1}^{N} \hbar\omega_i \hat{a}_i^\dagger \hat{a}_i + \sum_{\langle i,j \rangle} \hbar J_{ij}\left(\hat{a}_i^\dagger \hat{a}_j + \hat{a}_i \hat{a}_j^\dagger\right) \tag{2.5}$$

where $\omega_i = \sqrt{(C^{-1})_{ii}(L^{-1})_{ii}}$, $J_{ij} = \frac{(C^{-1})_{ij}}{2\sqrt{(C^{-1})_{ii}(C^{-1})_{jj}}}\sqrt{\omega_i\omega_j}$ and where we have neglected the zero field energy for convenience. Moreover, the sum $\sum_{\langle i,j\rangle}$ implies that we count each coupling only once as $J_{ij} = J_{ji}$. While this equation seems identical to a linear chain of coupled LC resonators [8], there is one crucial difference: J_{1N} is on the order of nearest neighbour coupling terms such as J_{23} and J_{56} instead of diminishing with increasing N.

To illustrate the above expression, we can write the Hamiltonian for our CQ system as as $\mathcal{H} = \hbar A^\dagger \underline{H} A$ with $A = (\hat{a}_1, \hat{a}_2, \hat{a}_3, \hat{a}_4)$ a column vector, $A^\dagger = \left(\hat{a}_1^\dagger, \hat{a}_2^\dagger, \hat{a}_3^\dagger, \hat{a}_4^\dagger\right)$ a row vector and

$$\underline{H} = \begin{bmatrix} \omega_1 & J_{12} & J_{13} & J_{14} \\ J_{12} & \omega_2 & J_{23} & J_{24} \\ J_{13} & J_{23} & \omega_3 & J_{34} \\ J_{14} & J_{24} & J_{34} & \omega_4 \end{bmatrix} \tag{2.6}$$

One can observe that even though in our circuit model there is only direct coupling between nearest neighbours, our effective Hamiltonian also contains coupling terms of higher order.

2.3 Input-output Theory

Equipped with the Hamiltonian expressed in the language of second quantization, we can now move on to include coupling to the environment and internal losses. We thus again consider our system being coupled to a transmission line P (with characteristic impedance Z_C) through a capacitance C_κ, as well as having internal losses through resistances R_i. To characterize the coupling we will use input-output theory, which relates the field put into the system and the field coming out of the system. The first difference from the previous section is that we make the substitution $C_i \to C_i + C_{\kappa i}$ for every site i coupled to a transmission line P_i via a capacitance $C_{\kappa i}$. By doing so we effectively absorb the additional capacitance due to external coupling into the shunt capacitance itself.

We then look at our system in the Heisenberg representation and introduce the Langevin equations for non-unitary evolution [9]

$$\dot{\hat{a}}_i = -\frac{i}{\hbar}\left[\hat{a}_i, \mathcal{H}\right] - \frac{\kappa_i}{2}\hat{a}_i - \frac{\gamma_i}{2}\hat{a}_i + \sqrt{\kappa_i}\hat{a}_{\text{in},i} \tag{2.7}$$

where the first term describes the unitary evolution of the system, the second term describes the decay of the field at site i due to coupling to the transmission line, the third term describes the decay of the field at site i due to dissipation and the final term represents the external driving force coming in from the transmission line at site i. Through consideration of the

equations of motion of the system [8] one can find these terms to be given by $\kappa_i = \frac{(C^{-1})_{ii}}{K_i Z_C}$ and $\gamma_i = \frac{(C^{-1})_{ii}}{R_i}$. Here, $K_i(\omega) = 1 + (Z_c C_{\kappa i}\omega)^{-2}$, where ω is the angular frequency of the field input into the system.

In addition to the above equations, the system also has to obey the input-output boundary condition $\hat{a}_{\text{in},i} + \hat{a}_{\text{out},i} = \sqrt{\kappa_i}\hat{a}_i$. Combining this with the Langevin equations allows one to solve for the various $\hat{a}_i$ and in turn calculate the scattering matrix elements S_{ij} using the relation

$$S_{ij} = \frac{\hat{a}_{\text{out},i}}{\hat{a}_{\text{in},j}} = \frac{\sqrt{\kappa_i}\hat{a}_i}{\hat{a}_{\text{in},j}} - \frac{\hat{a}_{\text{in},i}}{\hat{a}_{\text{in},j}} \tag{2.8}$$

These complex valued, frequency dependent matrix elements $S_{ij}(\Omega)$ are the actual values obtained during our measurements. What they describe is the ratio of a signal being sent in at port j to the signal put out at circuit i, from the perspective of an external observer. In most of our systems we couple to a transmission line at a single site only, in which case we are dealing with $S_{11}(\Omega)$, better known as the complex valued reflection coefficient $\Gamma(\Omega)$.

If we now assume that we are dealing with classical signals we can assume ($\hat{a}_i(\omega) = a_i e^{-i\omega t}$, $\hat{a}_{\text{in}}(\omega) = a_{\text{in}} e^{-i\omega t}$) and we can solve the Langevin equations to find an expression for $\Gamma(\omega)$. To illustrate this, we look again at the CQ system of Figure 2.1: 4 coupled RLC resonators with periodic boundary conditions, coupled to a single transmission line. While the closed form expression of $\Gamma(\omega)$ in terms of the C_i and other parameters should exist, it is neither elegant nor insightful, consisting of many terms of various orders. Instead we gain insight into the physics by looking at a plot of the absolute part of the reflection coefficient $|\Gamma(\omega)|$ as a function of frequency, as shown in Figure 2.2. We see that even though four resonators are present in the system, only three distinct resonances are observed; this phenomena is investigated in the next section.

2.4 Degeneracies and Dark Modes

As seen in Figure 2.2, the absolute part of the reflection coefficient shows three resonances, while having four resonators in the system. A first investigation into why this occurs can be performed by looking into the eigenvalues of the Hamiltonian of the system, which we defined as $\mathcal{H} = \hbar A^\dagger \underline{H} A$ with $\underline{H}$ given by the matrix of Equation 2.6. Finding the eigenvalues of the Hamiltonian comes down to diagonalising this matrix. Like the closed form solution of the reflection coefficient, a closed form solution of the diagonalisation of this matrix does exist, but it is unnecessarily complicated. Instead we choose to look into the eigenvalues by evaluating them numerically, using the parameter values described in the figure caption of Figure

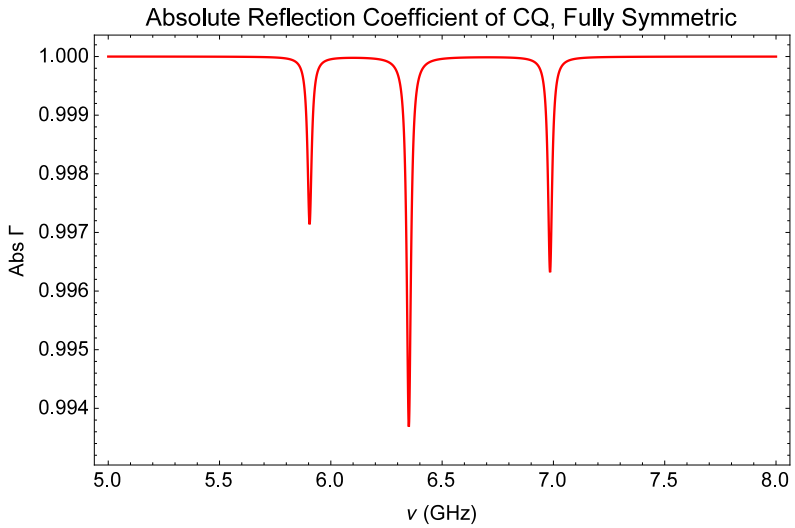

Figure 2.2: The absolute part of the reflection coefficient of the circular quatromer (CQ) system. Here we have taken $C_i = 300fF\ \forall i$, $C_{Ji} = 30fF\ \forall i$, $L_i = 1.74nH\ \forall i$, $R_i = 20k\Omega\ \forall i$, $C_\kappa = 2fF$ *and* $Z_c = 50\Omega$. *While there are four LC resonators present in the system, we see only three resonances.*

2.2. We find our matrix to have four eigenvalues, two of which are degenerate: $\lambda_1 = 5.91$ GHz, $\lambda_2 = 6.36$ GHz, $\lambda_3 = 6.36$ GHz, and $\lambda_4 = 6.99$ GHz. Two factors should be noted here. By defining $\underline{H}$ the way we did the eigenvalues have units of frequency and not energy, which would have been customary for a Hamiltonian. Moreover, we choose not to use units of angular frequency (in which way the second quantization Hamiltonian is defined), but instead divide by 2π to obtain regular frequency. These two changes allow one to verify that the eigenvalues are indeed the resonances observed in Figure 2.2 and are in line with the data obtained from measurements.

In order to think about where this degeneracy comes from we note that for this figure we have taken the parameter values to be equal between all four circuits, creating a high degree of symmetry that is broken only by the fact that one resonator is coupled to a transmission line. In the weak coupling regime, we can neglect this asymmetry and assume our system to be fully symmetric. Our system is then governed by the dihedral group $\mathcal{D}_n$: the group of symmetries of a regular polygon. This group of order $2n$ consists of the n reflections of the axes that pass through the fixed point of the system, as well as the n rotations $\mathcal{C}_n$. $\mathcal{C}_n$, also a group, then consists of all rotations about the fixed point by multiples of the angle $\frac{360\,\mathrm{deg}}{n}$, for a total of $2n$ symmetries. [10]

2.4.1 Eigenvector Analysis

For a system with such a high amount of symmetry it is not surprising to observe degeneracies. However, while the aforementioned degeneracy is indeed valid, further investigation shows that it is not crucial here for the disappearance of the fourth resonance. One can investigate this by breaking some of the symmetries. We can for example take $C_{1,3} = 0.9C_{2,4}$ while keeping all other values the same, creating a type of structure that has only n symmetries; $\frac{n}{2}$ reflection, and rotation symmetries. The eigenvalues are now no longer degenerate: $\lambda_1 = 6.00GHz$, $\lambda_2 = 6.35GHz$, $\lambda_3 = 6.64GHz$, and $\lambda_4 = 7.19GHz$. However, we observe that $|\Gamma(\omega)|$ remains the same on a qualitative level; there are still only three resonances as shown in Figure 2.3a. It appears that the resonance associated with λ_2 is not observed. We call this a dark mode of our system; a mode that cannot be excited. In order to investigate this further we look at the eigenvectors of the matrix $\underline{H}$ in the case of this diagonal pairwise symmetry. As eigenvectors of the Hamiltonian, they provide insight into the stationary states of the system and thus the time independent probability density of the wave function of the system. [11]

As shown in Figure 2.3b, we recognise four distinct eigenvectors: one for each eigenvalue as labelled by Roman numerals. While the first and last eigenvector are non-zero in all four components (each belonging to a resonator in the system), the two middle eigenvectors both have only two non-zero components. In the case of λ_2 the non-zero components correspond to resonators 2 and 4, while for λ_3 this holds for resonators 1 and 3. This means that these two eigenvectors belong to two different modes: for λ_2 the field will only populate resonators 2 and 4, while for λ_3 it will only populate resonators 1 and 3. Since we are driving the system at resonator 1, the mode corresponding to λ_2 is not excited, as this mode has no population at resonator 1. The mode is thus dark, giving us a spectrum with three resonances instead of four.

We now look at the above in more detail. Here we have a two fold symmetry of the system, between $C_{1,3}$ and $C_{2,4}$. This reduced the number of rotation and reflection symmetries by half, taking away the 90 and 270 degree rotation symmetries as well as the diagonal reflection symmetries. It appears that these symmetries are not essential for the system to have a dark mode. One can then investigate what happens when we take away even more symmetries. We do so by choosing a system for which $C_1 = 0.9C_{2,3,4}$ while keeping all other parameters the same. This leaves us with only two remaining symmetries: the trivial rotation symmetry of 360 degrees (which is always present) and the reflection in the axis through resonators one and three. Not shown in a figure, the system still retains the same spectrum of three resonances at similar eigenvalues as before, and again a dark mode.

If we are to explain the presence of a dark mode in the system through symmetries, it appears that the reflection symmetry in the axis through the coupled resonator is essential. In other words, from the perspective of a signal coming into the system at a specific resonator, there can be no difference traversing the system clockwise or anticlockwise. Combining this with the zero components of the eigenvectors gives the dark mode narrative the flavour of interference, where clockwise travelling and anti clockwise travelling waves destructively interfere at certain resonator sites. This could indeed cause the probability density of the field to be zero at the resonator sites, as found from the eigenvectors. While this seems like a possibility on an intuitive level, a more rigorous study of the physics of the system would be required to confirm this.

We can however check if the above symmetry is indeed mandatory by taking it away. To do so, we introduce a neighbouring pairwise symmetric system for which $C_{1,2} = 0.9C_{3,4}$ while keeping all other parameters the same. The system now again has one non trivial reflection symmetry, but in the diagonal, and again only the trivial 360 degrees rotation symmetry. The resulting spectrum is shown in Figure 2.3c, which now shows all four resonances. The eigenvalues are now $\lambda_1 = 5.99GHz$, $\lambda_2 = 6.46GHz$, $\lambda_3 = 6.53GHz$, and $\lambda_4 = 7.21GHz$. Moreover, all four eigenvectors now have four non-zero components as shown in Figure 2.3d. Indeed, removing the 1-3-axis reflection symmetry causes our system to no longer exhibit a dark mode. This fits our tentative picture of interference, as the clockwise path is different from the anticlockwise path.

It should be noted that during this thesis considerable time was also spent on experimenting with various ways of visualising the eigenvectors of a system with periodic boundary conditions. While not essential to the main thesis, various different forms are shown and discussed in appendix A.

We can also use a different tool than $|\Gamma(\omega)|$ to investigate the appearance and disappearance of the resonances. Instead of using a system that is coupled at only one resonator, we can instead couple it at different sites and look at the transmission scattering matrix elements. To illustrate this we will again use a circular quatromer like depicted in Figure 2.1, but now it will be coupled to four transmission lines: one at each resonator. Returning again to the case of $C_{1,3} = 0.9C_{2,4}$ while keeping all other parameters fixed, we can see what the various scattering matrix elements look like. Note that we choose the diagonal two-fold symmetry instead of the completely symmetric system to rule out any dependence on degeneracy of the eigenvalues. Depicted in Figure 2.4 are $|S_{11}|$ and $S|_{21}|$. While apparent from the definition of S_{ij}, it should again be noted that j is the input site and i is the output site.

In panel (a) we see the reflection coefficient as we saw it before: with three resonances. Comparing $|S_{11}|$ to $|S_{21}|$ in panel (b) we see that the same two

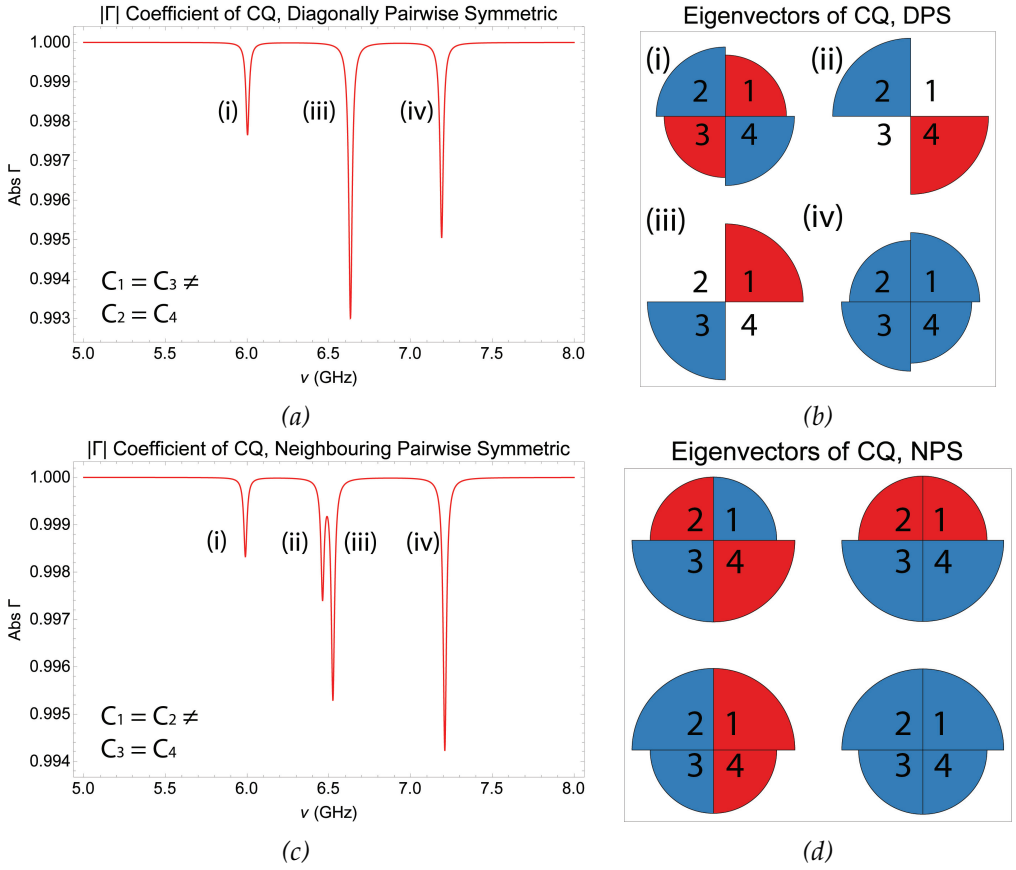

Figure 2.3: Absolute reflection coefficients and eigenvectors for different CQ systems. In the eigenvector plots each segment of the circle corresponds to the eigenvector component of a specific resonator. The color blue indicates a negative sign of the component while red indicates positive, and the area of the segment corresponds to the magnitude of the component. Moreover, the eigenvectors are ordered according to their eigenvalues, increasing from left to right as labelled by Roman numerals. This labelling is also present in the reflection coefficient plots, indicating which eigenvector corresponds to what resonance. Panel (a) shows $|\Gamma(\omega)|$ for a CQ system with a diagonally pairwise symmetry, while panel (b) shows the eigenvectors of the Hamiltonian of this system. Panel (c) shows $|\Gamma(\omega)|$ for a CQ system with a neighbouring pairwise symmetry, while panel (d) shows the eigenvectors of the Hamiltonian of this system.

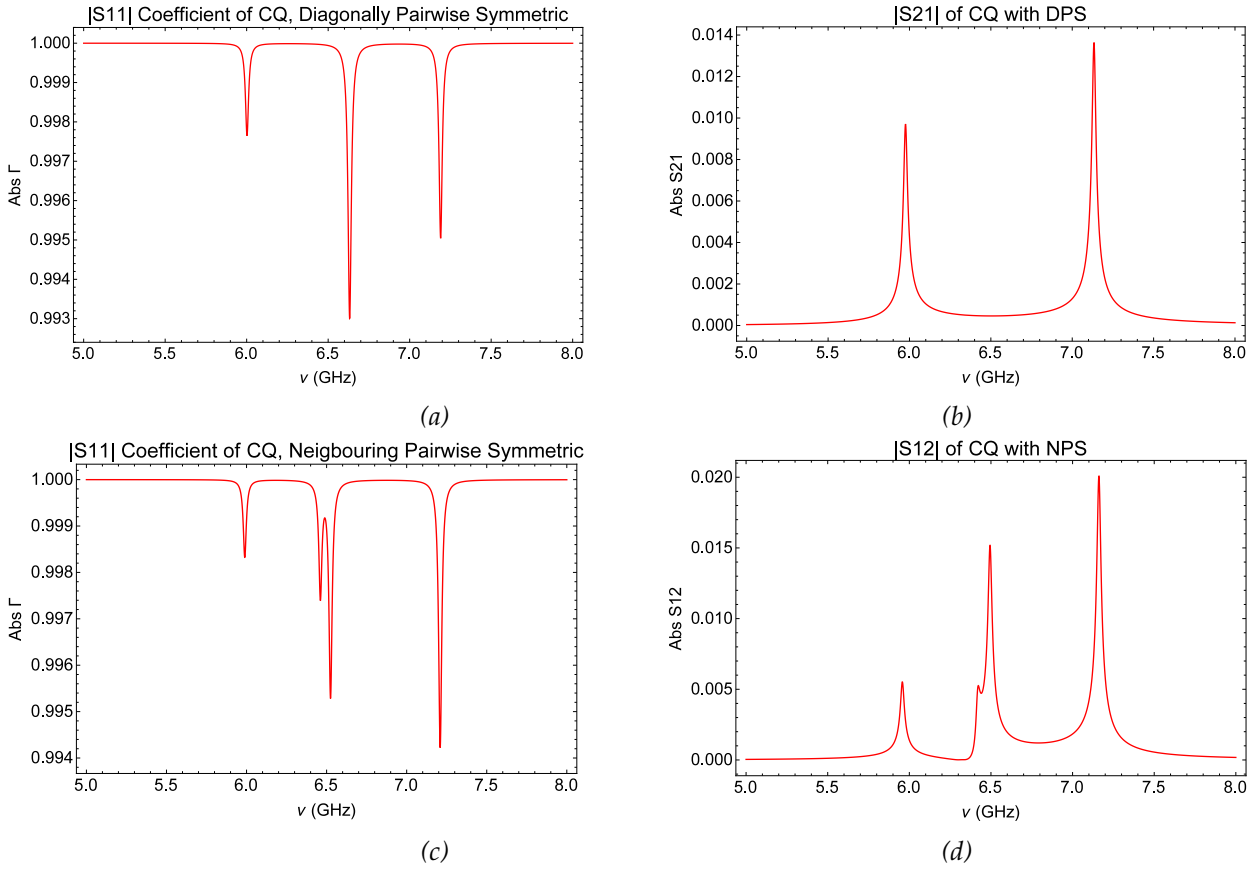

Figure 2.4: Different elements of the absolute value of scattering matrix S_{ij}. Panel (a) shows the previously depicted CQ system with diagonally pairwise symmetry in the reflection geometry, while panel (b) shows transmission from site 1 to 2 in the same system, showing two resonances. Panel (c) shows the previously depicted CQ system with neighbouring pairwise symmetry in the reflection geometry, while panel (b) shows transmission from site 1 to 2 in the same system, showing all four resonances.

outer resonances are present in both, at the same frequency. However, none of the two possible middle resonances are visible. This is as expected from our theory: driving the system at resonator 1 implies that the mode which only has a presence at resonators 2 and 4 cannot be excited, while the mode that only has a presence at resonators 1 and 3 has no output at resonator 2. If we instead look at the system with neighbouring pairwise symmetry ($C_{1,2} = 0.9C_{3,4}$) we again see a reflection spectrum with four resonances in panel (c), while (d) shows the transmission spectrum $|S_{12}|$. Here all four resonances are visible, as none of the eigenvectors have any zero components.

The previous findings pose somewhat of an issue for our measurements,

as we intend to fit parameter values to measurements of the reflection and transmission spectra. This is more difficult when one has less non-trivial data (in this case distinct resonances) to fit to. It does however mean that the number of resonances observed during the measurement gives us some initial information about the types of symmetries that are present in the system.

2.4.2 Dispersion Relation

In the previous section most of the discussion was about the CQ system, with four resonators. However, one can wonder if and how these effects generalize to systems of different numbers of resonators N, which is what we investigate here. We do so by diagonalising the previously derived Hamiltonian for N resonators in the second quantization framework

$$\mathcal{H} = \sum_{i=1}^{N} \hbar\omega_i \hat{a}_i^\dagger \hat{a}_i + \sum_{\langle i,j \rangle} \hbar J_{ij} \left(\hat{a}_i^\dagger \hat{a}_j + \hat{a}_i \hat{a}_j^\dagger \right) \tag{2.9}$$

which was valid for N coupled LC resonators, in the absence of external coupling or internal losses. In this process we aim to elucidate the occurrence of the degeneracies and their relationship to the number of resonators present in the system.

The above Hamiltonian is not trivial to diagonalise; to do so we first look at a simplified version

$$\mathcal{H} = \hbar\omega_0 \sum_{i=1}^{N} \hat{a}_i^\dagger \hat{a}_i + \hbar J \sum_{i=1}^{N} \left(\hat{a}_i^\dagger \hat{a}_{i+1} + \hat{a}_i \hat{a}_{i+1}^\dagger \right) \tag{2.10}$$

This corresponds to a case where every LC circuit is identical and thus has the same resonance frequency ω_0, while every coupling capacitance is also equal, leading to a single nearest neighbour coupling parameter J. Higher order neighbours are neglected in this approach. As the form of second and third term might suggest, it is useful to introduce the Fourier transformation of the creation and annihilation operators similar to how one derives band structures in introductory solid state lectures [12]

$$\hat{a}_m^\dagger = \frac{1}{\sqrt{N}} \sum_{k=1}^{N} \hat{b}_k^\dagger e^{\frac{-2\pi i m k}{N}} \tag{2.11}$$

$$\hat{a}_m = \frac{1}{\sqrt{N}} \sum_{k=1}^{N} \hat{b}_k e^{\frac{2\pi i m k}{N}} \tag{2.12}$$

The reason we choose to use a non standard (but valid) definition of the Fourier transform is because this is the variant implemented by Mathematica, which will simplify our work along the way. By substituting the transformations into Equation 2.9 we find that our Hamiltonian can be reduced

to

$$\mathcal{H} = \sum_{k=1}^{N} \hbar\varepsilon(k)\hat{b}_k^\dagger \hat{b}_k \tag{2.13}$$

where the dispersion relation $\varepsilon(k)$ is defined as

$$\varepsilon(k) = \omega_0 + 2J\cos\left(\frac{2\pi k}{N}\right) \tag{2.14}$$

Similar to how the Hamiltonian defined in Equation 2.9 could also be written as $\mathcal{H} = \hbar A^\dagger \underline{H} A$ with $A = (\hat{a}_1, ..., \hat{a}_N)$ a column vector, $A^\dagger = (\hat{a}_1^\dagger, ..., \hat{a}_N^\dagger)$ a row vector and $\underline{H}$ a non-diagonal matrix we can write Equation 2.13 as $\mathcal{H} = \hbar B^\dagger \tilde{H} B$ with $B = \left(\hat{b}_1, ..., \hat{b}_N\right)$ a column vector, $B^\dagger = \left(\hat{b}_1^\dagger, ..., \hat{b}_N^\dagger\right)$ a row vector and $\tilde{H}$ a diagonal matrix. We have thus successfully diagonalised our Hamiltonian, and obtained its dispersion relation. While this expression is of interest by itself, it is but an approximation of our true system of N coupled resonators. This system includes more than just nearest neighbour coupling and not every LC circuit has to be identical. While we now turn to this first issue, it is important to note that we will not expand our model to contain the second. If the LC circuits (as well as the capacitances coupling them) are not identical, the translational symmetry of the system is broken, in which case we thus do not have a translation invariant system. This implies that the mode number k is no longer a good quantum number, in analogy to the crystal momentum from solid state theory. Our approach would therefore no longer be valid. However, as we will see, we can still obtain information also of importance for systems without translational invariance.

In order to incorporate higher order coupling than just nearest neighbour we return to the second term of Equation 2.9. We can see that there is a summation over $i \neq j$ which means it includes every type of coupling, not just nearest neighbour. But now we note that our approach to solving the nearest neighbour Hamiltonian is not unique to this type of coupling: the same solution for the dispersion relation would hold for next nearest neighbour coupling, except that in Equation 2.10 $(i+1)$ would become $(i+2)$, which means that the dispersion relation would contain $\cos\left(\frac{4\pi k}{N}\right)$ instead of $\cos\left(\frac{2\pi k}{N}\right)$. The same holds for third nearest neighbours, and so on. The dispersion relation of our actual Hamiltonian of Equation 2.9 contains a summation of all of these terms.

However, one has to take care when it comes to the pre factor of the aforementioned cosine terms, $2J$ in our simplified relation. For this we use that we again assume complete symmetry, meaning that we can take $J_{12} = J_{23}$ and so on. We denote this type of nearest neighbour coupling as first order coupling J_1, which generalises as expected: next nearest neighbour coupling is J_2, and Nth order coupling is J_N.

We then have to consider the case of even and odd N separately. For even N, given one resonator, there are $N-1$ other resonators, which is an odd number. There are two at each distance up to $\frac{N}{2}-1$ and one at distance $\frac{N}{2}$. This means that if we count the number of the nearest neighbours, all N resonators have two of them. However, by summing all of these we count each pair twice; the total number of nearest neighbour coupling terms J_1 is therefore N. The same holds for any order of coupling, except for the highest order: $\frac{N}{2}$th order coupling $J_{\frac{N}{2}}$. Here, each point has only one $\frac{N}{2}$th order neighbour, while we still count each pair twice. Therefore there are $\frac{N}{2}$ coupling terms $J_{\frac{N}{2}}$ in our summation. What this implies is that the first $\frac{N}{2}-1$ cosine terms will have the pre factor of 2 times the respective coupling term (as the summation over N is exactly cancelled out by the normalization of the Fourier transform), while the final term has a pre factor that is half this and thus simply the coupling term $J_{\frac{N}{2}}$ itself.

For odd N the situation is simpler. For odd N, given one point, there are $N-1$ other points, which is an even number. There are two at each distance up to $\frac{N-1}{2}$, so each term has the same pre factor of 2 times the coupling term. This leads to the follow two dispersion relations, for even and odd N respectively

$$\varepsilon(k)_{even} = \omega_0 + \sum_{l=1}^{\frac{N}{2}-1}\left[2J_l \cos\left(\frac{2\pi lk}{N}\right)\right] + J_{\frac{N}{2}}\cos(\pi k) \tag{2.15}$$

$$\varepsilon(k)_{odd} = \omega_0 + \sum_{l=1}^{\frac{N}{2}-1} 2J_l \cos\left(\frac{2\pi lk}{N}\right) \tag{2.16}$$

which can be put into the derived Hamiltonian

$$\mathcal{H} = \sum_{k=1}^{N} \hbar\varepsilon(k)\hat{b}_k^\dagger \hat{b}_k \tag{2.17}$$

To illustrate the above, we take the example the circular hexamer (CH, $N = 6$) which has the dispersion relation

$$\varepsilon(k) = \omega_0 + 2J_1 \cos\frac{\pi k}{3} + 2J_2 \cos\frac{2\pi k}{3} + J_3 \cos\pi k \tag{2.18}$$

We have now diagonalised the Hamiltonian of our fully symmetric coupled system of N LC resonators and by doing so related the eigenvalues of the Hamiltonian to the mode number k. Next we turn to relating k to the eigenvectors. To do this, we compare the expressions $\mathcal{H} = \hbar A^\dagger \underline{H} A$ and $\mathcal{H} = \hbar B^\dagger \tilde{H} B$. The process of diagonalising a matrix tells us that $\underline{H} = X^\dagger \tilde{H} X$, where X is a unitary matrix. Inserting this into the above gives $\mathcal{H} = \hbar A^\dagger \underline{H} A = \hbar A^\dagger X^\dagger \tilde{H} X A = \hbar B^\dagger \tilde{H} B$ and thus that $\hat{b} = X\hat{a}$. If we now

recall equations 2.11 and 2.12 we see that X is in fact the Fourier transformation. This tells us that if we want to find how the mode number k is related to the eigenvector of each eigenvalue, we have to compute the Fourier transform of said eigenvector and find for which k the transformation is nonzero; this is the k value belonging to that eigenvector.

We perform the above transformations for the eigenvectors of the circular trimer (CT), circular quatromer (CQ), circular pentamer (CP) and circular hexamer (CH) and plot the calculated k values along with the associated eigenvalue in the same figure as the dispersion relations of equations 2.15 and 2.16 in Figure 2.5. There are three things to note here: we again choose to divide by 2π in order to obtain regular frequencies, and we shifted the k values back by one. This has to do with the way in which Mathematica defines the Fourier transform [13]. Moreover, the eigenvectors belonging to the degenerate modes take on a nonzero value at both k values; we simply choose a unique k for each of the eigenvectors as the distinction is arbitrary.

A few phenomena can be observed in Figure 2.5. The first is the number of degenerate eigenvalues: both CT and CQ have two degenerate eigenvalues, corresponding to a $|\Gamma(\omega)|$ spectrum of two and three resonances respectively, as was observed for the fully symmetric CQ system (Figure 2.2). The CP and CH system however have two sets of pairwise degenerate eigenvalues, corresponding to 3 and 4 visible resonances. In the previous section we established it is not the degeneracy itself that causes the disappearance of the resonances but in fact the position of non-zero elements in the eigenvectors. However, we have also established that it is one of the two previously degenerate modes that is dark. We thus hypothesize that counting the degeneracies in the fully symmetric case can tell us how many resonances to expect in systems that retain their clockwise and anticlockwise traversing symmetry, even in the absence of full translational invariance.

To see how this pattern of degeneracies comes about we can take a closer look at the figures and observe that in panel (a) we see one high frequency mode and two degenerate middle frequency modes, while panel (b) shows the same modes plus an additional low frequency one. In panel (c) we observe that the previously lonesome low frequency mode now also becomes degenerate, and in panel (d) we see yet another non-degenerate lower frequency mode added. One can understand this by looking at figure: in the case of even N the lowest frequency mode belongs to an equal number of eigenvalue elements pointing up and down, effectively cancelling each other out energetically and giving a low frequency, such as in a spin system. In a system with odd N such a mode does not exist, and hence neither does the lonesome low frequency mode. However, as stated before, one can hope to gain a more fundamental understanding of these emergences and disappearances by studying the physics of the system on a more formal level.

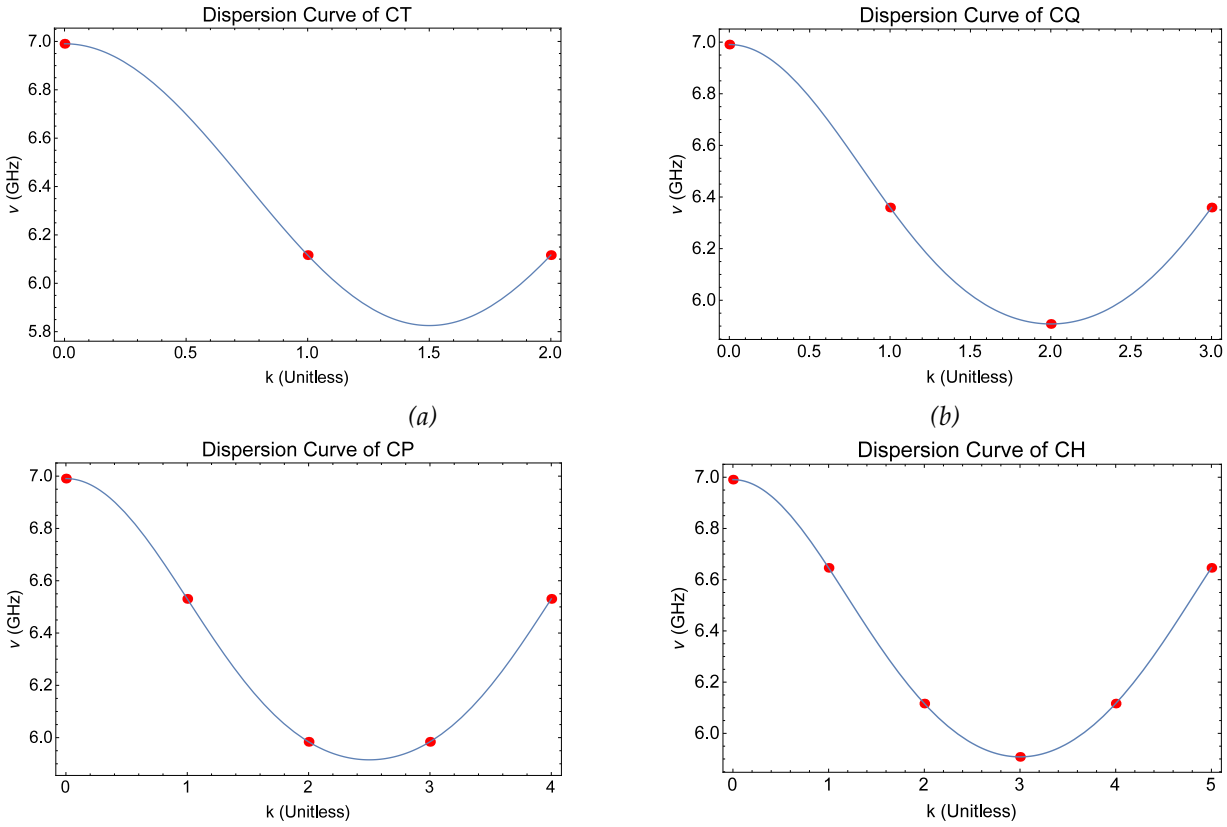

Figure 2.5: Four panels showing the relationship between the mode number k maximizing the Fourier transform of the eigenvectors and the eigenvalues (red circles), as well as the derived dispersion relations between k and the same eigenvalues (blue curves). For each panel we have taken $C_i = 300\ fF\ \forall i$, $C_{Ji} = 30\ fF\ \forall i$, $L_i = 1.74\ nH\ \forall i$, $R_i = 20\ k\Omega\ \forall i$, $C_\kappa = 2\ fF$ and $Z_c = 50\ \Omega$. Panel (a) shows the circular trimer, panel (b) the circular quatromer (CQ), panel (c) the circular pentamer (CP) and panel (d) shows the circular hexamer (CH).

Nevertheless, with the above information we can make a statement about the least amount of resonances expected in $|\Gamma(\omega)|$ for the various systems to be measured: we expect at least $\frac{N}{2} + 1$ resonances for systems with even numbers of resonators N and $\frac{N}{2} + \frac{1}{2}$ for odd N. Observing more than the listed amount of resonances appears to indicate that the system is not symmetric in the axis through the coupled resonator, which can also be valuable information with respect to fabrication quality.

Chapter 3

Experimental Setup

In this chapter we first discuss the devices that will be used, including a brief description of their composition as well as how each devices differs from the others. We then move on to the actual measurement process, giving a summary of the important steps as well as the apparatuses used. Finally we describe how we fit the obtained data with the previously described theoretical model in order to obtain the relevant parameters.

3.1 Devices Studied

As discussed before, this thesis studies coupled lumped-element resonators with periodic boundary conditions. In chapter 2 we immediately made the simplification of describing the system in the circuit framework, treating it as an RLC circuit. In reality however these elements have to be constructed using fabrication techniques. While the actual fabrication process and considerations that come with it were not part of this thesis, we still provide a brief description of the different tools and components used.

3.1.1 Components of the Devices

The circuits themselves are fabricated into a layer of niobium on top of a sapphire substrate using a photolithographic process, with respective layer thicknesses of 150 nm and 0.43 mm. [1] The choice for niobium stems from the fact that it becomes superconducting at around 9.2 K. Since we perform our measurements at liquid helium temperatures, the layer will be dissipationless and not contribute to resistance based losses. [1] It is in this superconducting layer that we then construct the different components such as C_i, L_i, C_{Ji} and C_κ. A micrograph picture of a fabcricated circular quatromer is shown in Figure 3.1 (a).

The individual components are created using two types of 2 dimensional structures: inter-digital capacitors and meander inductors. The inter-digital capacitors are a periodic structure of multiple fingers. Their capacitance comes from the gap between the fingers, and thus one chooses long and meandered gaps to maximize the area [1]. All three types of capacitances of our circuit model are constructed in this way. C_i is often referred to as the shunt capacitor, while C_{Ji} and C_κ are coupling capacitors. They are depicted in Figure 3.1 (d), (c) and (b) respectively. There are various ways to increase the capacitance of such a finger structure. The method employed for these experiments is increasing the number of fingers and thus the number of gaps, which then results in a higher capacitance. Indeed, when we study samples in which we for example vary C_i, it is the number of fingers fabricated that changes from device to device. Finding a recipe for how the relevant parameters vary when changing the number of fingers for the different capacitors is one of the main goals of this thesis. We should note that this is not exactly true for C_κ. Here one connects the transmission line to the shunt capacitor through a single capacitance finger, and it is in fact the ratio of this finger's length to the shunt capacitor fingers that is the parameter that is varied in fabrication.

The inductors L_i of our devices are meander line inductors. They consist of conductor line that is meandered back and forth over the structure to maximize its length, and with that its inductance [1]. Throughout all of the devices used in this thesis the inductance is kept fixed on the fabrication side, and we thus also assume so during our analysis. Figure 3.1 (e) depicts one of these meander line inductors. It should be noted that we do not mention a built in resistor, as we do not put one into the system. The reason that our description of the system includes a resistance component is because in reality such a device always has some internal resistance, for example from sources such as dielectric losses in the capacitor electric fields. [1]

3.1.2 Geometries and Fabrication Variations

In chapter 2 we gave various examples and figures for one particular device, the circular quatromer (CQ) with 4 resonators. However, in our experiments we used a variety of such devices: in addition to CQ we also studied the circular trimer (CT) with $N = 3$, the circular hexamer (CH) with $N = 6$ and the circular octomer (CO) with $N = 8$. But we did not only study how changing the number of resonators changes the system. We also looked at how changing the individual parameters C_i, C_{Ji} and C_κ changed the system, in addition to varying how many of the resonators are connected to a transmission line. As previously stated, this is the main goal of the thesis: quantifying how changing these parameters from a fabrication viewpoint (number of fingers in the capacitor, number of transmission lines connected) affects the internal

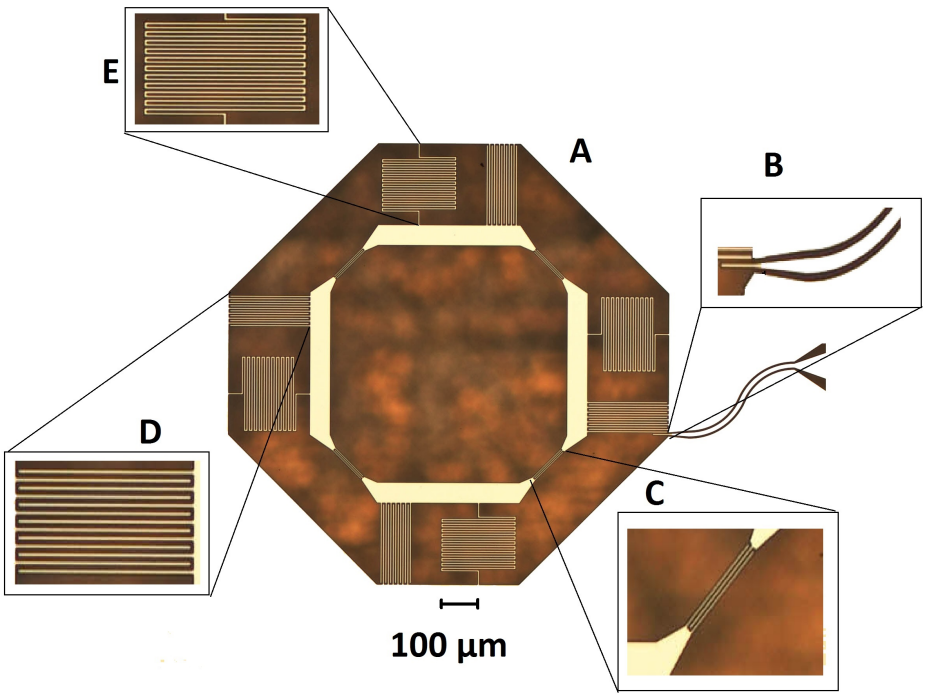

Figure 3.1: A micrograph image of a circular quatromer device. Panel (a) shows the entire device with all four resonators and a single transmission line, while panel (b) shows how the transmission line is coupled to the first resonator using coupling capacitor C_κ, which is a single finger. Panel (c) shows the coupling capacitor C_{Ji} that couples the different resonators through the central island, and panel (d) shows the capacitance C_i, the shunt capacitor. Finally, panel (e) shows the meander line inductor L_i. The plane around the structure is the ground.

parameters, such as the coupling J.

An example of this would be CQC, for which we have 6 different devices with all equal parameters, except for C_i. C_i is varied between the devices by changing the number of shunt capacitor fingers, and thus the resulting devices should have different internal parameters. Another example is shown in Figure 3.2, which is an illustration of a CQ circuit connected at all 4 resonators next to a CQ circuit connected at only one.

3.2 Dipstick Measurements

All measurements described in this thesis were performed using a dipstick measurement, submerging the device into a liquid helium dewar to cool them down to 4.2 K. The device itself was placed onto the dipstick, and the other side of the dipstick was connected to a vector network analyzer (VNA)

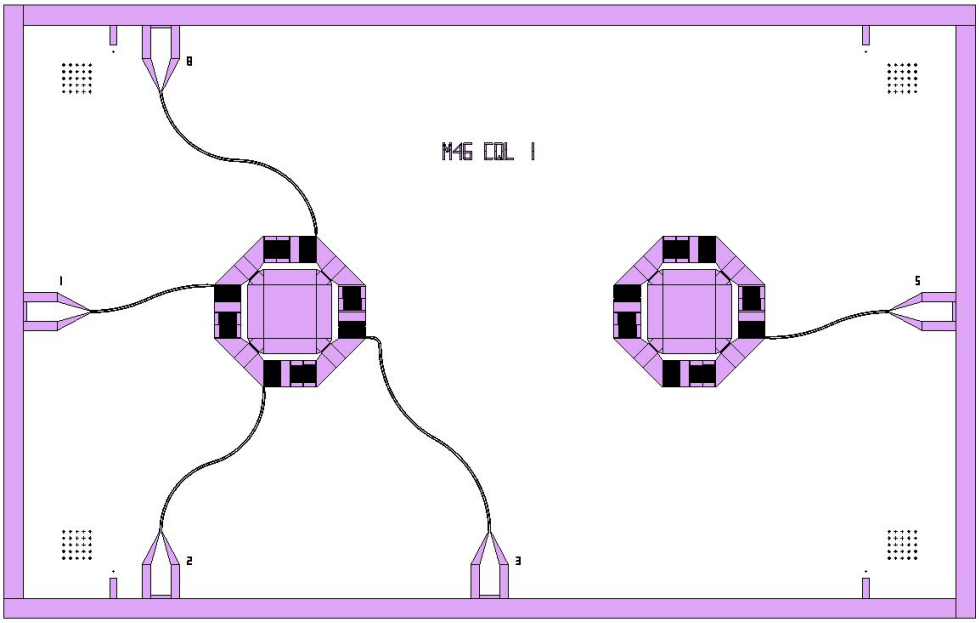

Figure 3.2: An illustration of the chip on which these particular CQ structures are printed. One is connected to four transmission lines, while the other is connected to only a single one.

using SMP connectors. The VNA then performed the actual measurement of the reflection and transmission coefficients, which we then stored and analyzed.

Different steps have to be taken in order to measure with the dipstick setup. To begin with one performs a calibration of the VNA and the SMP cables connected by connecting them only to the dipstick and no device. This is done to calibrate out any distortions caused by the cables. The calibration is done manually, using a specifically designed calibration kit containing four components: a short, a load, an open and a through connector. Guided by the VNA, one connects these components to the corresponding cable port on the dipstick one by one, after which the VNA gathers statistics for its calibration settings. As one of the VNA ports was not functional, we could only use three out of four, which meant 11 measurements had to be performed for the calibration: short load and open on each of them, and a through connection from the first to the second and the first to the third connected cable. As one has to constantly change the connections on the bottom of the dipstick the calibration cannot be done at liquid helium temperatures, which has to be taken into account during the data analysis.

Depending on the orientation of the devices on each chip (such as shown in Figure 3.2) one might have to change the ports to which the SMP cables

are connected on the dipstick between measurements. Every time this is done one should re-do the calibration, in order to combat unwanted noise as much as possible. It should be noted that this is not the only option: one can also rotate the device on the dipstick itself, changing which parts of the chip are connected. It is up to the user to decide which approach is more efficient as doing the calibration takes time, but so does waiting for the dipstick to get back to room temperature in order to rotate the device.

Once the calibration has been completed, one can mount the device and begin the submerging procedure. The dipstick is slowly placed into the helium dewar, keeping a constant eye on the pressure. While initially not much happens, there comes a certain point at which the pressure rapidly increases: here more than before it is crucial to take your time and let the pressure drop before submerging the dipstick any further. This is mainly for safety considerations, as when the pressure becomes too high the dipstick might be rapidly ejected. Once the device becomes sufficiently cooled, resonances will appear on the VNA; a sign that temperatures have become low enough to induce superconductivity. Once this happens one should still lower the device several centimeters further in order for the temperature of the device to stabilize as much as possible.

Once the resonances are visible on the VNA, the measurement process moves over here. One might initially have to change the frequency range to see all resonances, after which we choose to zoom in on a region of 200 MHz below and above the first and last resonance respectively. While one can choose which scattering matrix elements to display on the VNA itself, saving the data saves the entire matrix. This is done either saving both the real and imaginary parts or the absolute part and the phase. Once the measurement is completed, we slowly take the dipstick out of the dewar again. However, before doing so completely we leave it inside somewhere above the liquid helium level, indicated by the disappearance of the resonances on the VNA. We then also save the scattering matrix elements for the device at this position, giving us a high temperature dataset. This is done in order to compensate for calibrating at room temperature.

3.3 Fitting the Data

In the previous section we have discussed how we perform the experiments and gather the data. We now turn to analyzing the data and fitting it to the model developed in chapter 2. As the majority of the devices measured are coupled to a single transmission line, most of this section is devoted to measurements of the reflection coefficient $\Gamma(\omega)$. We first take into account that calibration is done at room temperature while measurements are done at liquid helium temperatures. To do so, we divide our liquid helium data

by the data taken at high temperature: the goal of this is to normalize the coefficient so that the coefficient takes the value 1 in the absence of any resonances.

Once this has been completed we attempt to isolate the resonances from the data. This is essential for this fitting procedure, as there are many data points away from the resonances that do not need to be fit, which otherwise compete with the important data in the fitting algorithms. This is done using Mathematica's built in *FindPeaks* function, which allows one to find the various local minima in the data.

Having isolated the data of the resonances, a fitting algorithm can be used to find the set of parameters that best fits the data given a model. However, which model to use is not entirely obvious. In chapter 2 we successfully constructed an expression for $\Gamma(\omega)$ in terms of the parameters C_i, C_{Ji} and so on. This was a highly complicated model involving matrix inversions and solving systems of equations. Moreover, it was a model of many parameters: all the capacitances, the inductances and the resistances, many of which are not set in stone for each device. Even if one uses previous research into the results of the fabrication to obtain initial guesses for these parameters, fitting such a large amount of parameters using a model this complicated to a dataset with only a few features is not feasible.

Instead we choose to fit our devices according to the resonance frequencies ω_i, the coupling terms J_{ij} and the dissipation terms κ_i and γ_i. Doing so eliminates part of the complexity of the model and even allows Mathematica to find closed form solutions of $\Gamma(\omega)$ to fit to. However, this is still a large number of parameters: for the CQ system coupled at 1 resonator one has four ω_i and γ_i terms, one κ term and 8 J_{ij} terms. Here fabrication considerations provide some relief however. For each device constructed, no deliberate asymmetry is introduced. This means that, up to fabrication errors, C_i, C_{Ji}, L_i, R_i and C_κ are all constant for all i (but not necessarily equal to one another) in each individual circuit. If this holds it simplifies the situation greatly, as for example $J_{12} = J_{23}$. Sadly, after the fabrication of these particular samples it was discovered that there is an accidental asymmetry present in the system. This is most likely because of the way horizontal and vertical capacitances are written onto the substrate; drawing the same capacitor at a different angle results in a different capacitance due to a so far undetermined error. It seems likely that this is due to how we fabricate the capacitances, but asymmetries in the substrate are also not excluded.

How problematic this is depends on the number of resonators present in the system as well as its geometry. For example, for $N = 4$ this would lead to the diagonally pairwise symmetry discussed in chapter 2, in which case there will still be dark modes in the system. However, for $N = 6$ for example, this could already break the symmetry between traveling clockwise and

anticlockwise, depending on the magnitude of the discrepancy.

While it is certainly unfortunate, we can still simplify our model somewhat. For the CQ system coupled to a single line, we assume it to evolve according to the Hamiltonian

$$\underline{H} = \begin{bmatrix} \omega_{13} & J_{NN} & J_{NNN} & J_{NN} \\ J_{NN} & \omega_{24} & J_{NN} & J_{NNN} \\ J_{NNN} & J_{NN} & \omega_{13} & J_{NN} \\ J_{NN} & J_{NNN} & J_{NN} & \omega_{24} \end{bmatrix} \tag{3.1}$$

As seen here, we assume that both horizontal resonators have the same resonance frequency ω_{13}, and similarly for the vertical ones ω_{24}. Furthermore we assume that all nearest neighbour couplings J_{NN} are equal, and the same for next nearest neighbour coupling J_{NNN}, as a first order approximation. Finally we have only one κ term which we assume to be independent of frequency (in reality there is a weak dependence), and finally we assume equal γ_i terms for all resonators. While this is involves quite an extensive series of simplifications, there are not many other options; a larger collection of parameters quickly leads to an under determined fitting routine, especially when one has only three resonances due to the dark mode.

Now that we have decided on a model, there is another factor to consider: what dataset we want to fit. We have access to the real, imaginary, absolute and phase part of the data, or any combination of these. It is desirable to fit all of these, but so far we have only adapted the fitting procedure to work with the absolute part. This is due to limited time available in combination with the difficulty of finding good initial parameter values for each type of data, which we turn to next. In the future one might however try to include these other types of data in order to obtain better estimates.

Nevertheless, even when taking the absolute spectrum finding initial parameters is of importance. After different types of strategies we arrived at the conclusion that by simplifying the Hamiltonian of 3.1 even further we can obtain initial parameter values that are good enough to have the fitting procedure converge to a satisfactory level for almost all of our CQ datasets. What we do is we also assume $\omega_{13} = \omega_{24} = \omega_0$ and look at the eigenvalues of this system. One obtains four eigenvalues, corresponding to the four resonances, two of which are degenerate. As this system contains only three parameters (ω_0, J_0 and J_1) and we find three distinct eigenvalues, we can solve the system and obtain our initial guesses on the basis of the locations of the resonances in the measured data. This is also the reason why we cannot have ω_{13} and ω_{24} as distinct parameters and still solve for the initial parameter values: with the dark mode present in the system, we would have three equations (eigenvalues) to determine four variables (the parameters).

For γ and κ we use that on the basis of their emergence in the equations they seem to be the dominant factor in determining full-width-half-maximum of the resonances, which we can find from the data. Moreover, they also determine the coupling depths. In order to find an initial estimate for these parameters we thus evaluate our simplified $|\Gamma(\omega)|$ at one of the resonances and solve the resulting system in terms of the already determined parameters as well as the coupling depth of the resonance and the full-width-half-maximum. In this way we obtain our initial guess for γ and κ.

To give an indication of how well this entire routine works, Figure 3.3 shows the data and corresponding fit of a measurement performed on a CQ device, specifically from the CQJ sample (where we vary coupling capacitances). As can be seen, the data indeed shows three resonances as expected from the diagonally pairwise symmetric geometry, and the fit reproduces all important qualitative features, such as number of resonances, relative peak height and position. One downside of the approach used is that we do not have a reliable estimate for the error in the fitted parameters. While Mathematica does give confidence intervals, we have found these to give error estimates on the order of less than a tenth of a percent, which is highly unlikely. This leaves us in the awkward position of reporting values without error bars, something we touch on during the discussion of the results in the next chapter.

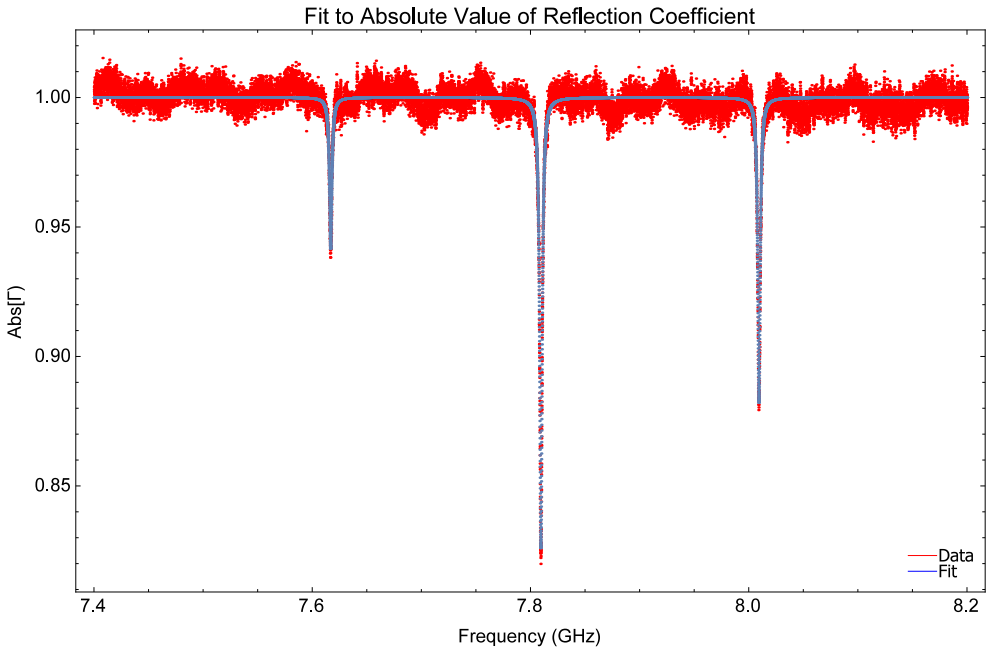

Figure 3.3: A fitted dataset of a circular quatromer. All qualitative features such as peak location and relative height are reproduced to relatively high precision. For this fit, the parameter values found are $\omega_{13} = 2\pi \times 7.85$ GHz, $\omega_{24} = 2\pi \times 7.71$ GHz, $J_{NN} = 92.1$ MHz, $J_{NNN} = 35.7$ MHz, $\gamma = 2.60$ MHz and $\kappa = 0.490$ MHz.

Chapter 4

Results and Discussion

In this chapter we report and discuss the findings of our measurements. While it may seem most sensible to start with the structure with either the lowest or highest number of resonators, we instead choose to start with the circular quatromer. This is because here we had by far the most different samples to look at.

4.1 Circular Quatromer

All circular quatromer (CQ) samples studied are variants of a standardized CQ circuit, the fabrication details of which are as follows: C_κ is made with a capacitance finger fraction of 0.2, C_{ji} with 3 fingers, C_i with 20 fingers and inductor L_i with 22 windings. In total we had four different types of CQ samples: one where we vary C_i, denoted CQC, one where we vary C_{ji}, denoted CQJ, and one where we vary C_κ, CQK, all of which are connected to a single transmission line. We also had a chip on which we looked at CQ connected at all four resonators, denoted CQL. The standard circuit is present on all 4 different samples for comparison. Moreover, following the discussion of the two fold symmetry in chapter 2, we expect all CQ circuits to exhibit three resonances, with the fourth one being dark.

4.1.1 CQJ

We begin with the sample on which we vary C_{ji}, denoted by CQJ. As described in chapter 3 the fabrication parameter being varied in order to influence C_{Ji} is the number of capacitor fingers, here varied between 2 and 10 in a total of six circuits. We find that each of them exhibits three resonances. This is as expected because our system should have the diagonally pairwise symmetric geometry due to the discrepancy between horizontal and vertical capacitances. Moreover, we are able to fit the spectra of each resonator to good qualitative accuracy, and the fitted values are listed in Table 4.1. The

parameter trends are as expected: increasing C_{Ji} effectively increases the capacitance of nearby resonators, thus lowering their resonance frequency, while it increases the nearest and next nearest neighbour coupling strengths. Similarly, both γ and κ should weakly decrease with increasing coupling capacitance elsewhere in the system. Furthermore the fits indeed confirm that for each resonator $\omega_{1,3} \neq \omega_{2,4}$, as expected. Important is to note that for the resonator with the lowest coupling capacitance we did not vary the number of fingers, but instead the gap between two of them. Furthermore there is one caveat to the parameter values of Table 4.1 and that is that we do not have error estimates. One approach would be to simply fabricate N identical samples to collect statistics; this is however resource and time consuming.

Fingers	ω_{13} (GHz)	ω_{24} (GHz)	J_{NN} (MHz)	J_{NNN} (MHz)	γ (MHz)	κ (MHz)
$10\mu m$	$2\pi \times 7.85$	$2\pi \times 7.71$	92.1	35.7	2.60	0.490
2	$2\pi \times 7.70$	$2\pi \times 7.50$	156	55.4	2.41	0.501
3	$2\pi \times 7.61$	$2\pi \times 7.31$	213	90.6	2.62	0.464
4	$2\pi \times 7.46$	$2\pi \times 7.19$	273	94.8	2.44	0.438
6	$2\pi \times 7.26$	$2\pi \times 6.80$	354	167	2.08	0.367
10	$2\pi \times 6.94$	$2\pi \times 6.59$	494	195	2.07	0.351

Table 4.1: Fitted parameters for the CQJ samples.

We then look at what we want to extract from the fitted parameters. In these samples we vary C_{Ji} by changing the number of coupling capacitor fingers, and we aim to find a direct relationship between these two quantities. In order to do so we note that the dominant influence of C_{Ji} is on J_{NN}, and the relationship should thus be contained in this parameter. The exact form of the J coupling dependence on C_{Ji} is not trivial however; J_{NN} is defined through $J_{ij} = \frac{(C^{-1})_{ij}}{2\sqrt{(C^{-1})_{ii}(C^{-1})_{jj}}}\sqrt{\omega_i\omega_j}$ which also depends on the shunt capacitance C_i. The value of the shunt capacitance should be static for this sample as we do not vary its number of fingers, but the value is not accurately known beforehand. In order to circumvent this problem we fit not only the values of C_{Ji} but also the two values of C_i: $C_{1,3}$ and $C_{2,4}$. We do this by performing a joint fit on the data. We fit the measured $\omega_{1,3}$ and $\omega_{2,4}$ defined as $\sqrt{\frac{(C^{-1})_{ii}}{L_i}}$ together with the measured J_{NN} and obtain the three sets of parameters C_{Ji}, $C_{1,3}$ and $C_{2,4}$. As ω_i also depends on the inductance L_i we use that based on previous experiments [1] we expect it to have a value of approximately 1.84 nH. Moreover, we do not only use the fitted values from table 4.1 but also those of table 4.2. Described in the next section, these are the fitted values of $\omega_{1,3}$, $\omega_{2,4}$ and J_{NN} obtained from varying the number of shunt capacitance fingers on the CQC sample, giving us extra data points to

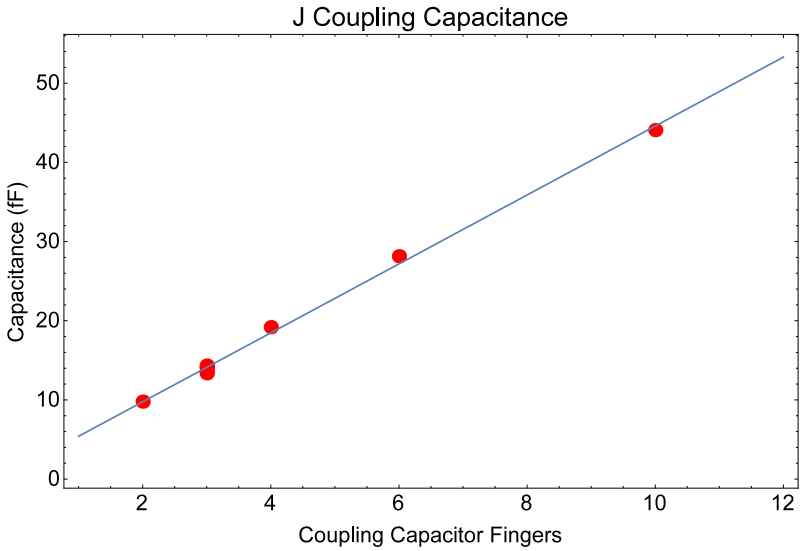

Figure 4.1: The fitted linear relationship between the number of coupling capacitance fingers and the coupling capacitance C_{Ji} obtained from the combined datasets of the CQJ and CQC samples.

use.

Figure 4.1 shows the obtained relationship between C_{Ji} and the number of coupling capacitor fingers. As expected from previous research [1] the data indicates that there is a linear relationship between the number of fingers and the resulting capacitance. The dependence found is $C_{Ji} = 1.05 + 4.35 \times \#fingers$ in units of fF. It should be noted that the large number of overlapping points at $n = 3$ coupling capacitor fingers are the data points from the CQC sample; the fact that they overlap shows of that the fit successfully reproduces approximately the same value of C_{Ji} for all of the circuits.

4.1.2 CQC

In analogy to the previous CQJ samples, the samples in which we vary the shunt capacitance C_i are denoted by CQC. Again the parameter variation on the fabrication side is due to changing the number of fingers in the capacitor. The expected and observed dependencies are now the same for all parameters: higher C_i leads to lower ω_i, γ and κ, J_{NN} and J_{NNN}. The fitted parameters are listed in Table 4.2.

While 6 sample with different C_i were available, only four could be fitted. This is because the two samples with the lowest shunt capacitance values displayed anomalous behavior, as shown in Figure 4.2 for the second lowest shunt capacitance (9 fingers). Their spectra showed anywhere from 3 to 6 resonances and in a circuit with 4 resonances we cannot find an obvious

Fingers	ω_{13} (GHz)	ω_{24} (GHz)	J_{NN} (MHz)	J_{NNN} (MHz)	γ (MHz)	κ (MHz)
5	-	-	-	-	-	-
9	-	-	-	-	-	-
13	$2\pi \times 8.75$	$2\pi \times 8.37$	220	127	3.40	1.10
16	$2\pi \times 8.23$	$2\pi \times 7.79$	252	132	2.73	0.591
20	$2\pi \times 7.58$	$2\pi \times 7.36$	212	61.9	2.73	0.472
24	$2\pi \times 7.09$	$2\pi \times 6.89$	177	56.2	2.05	0.321

Table 4.2: Fitted parameters for the CQC samples. The measurements of the samples with 5 and 9 fingers could not be fit.

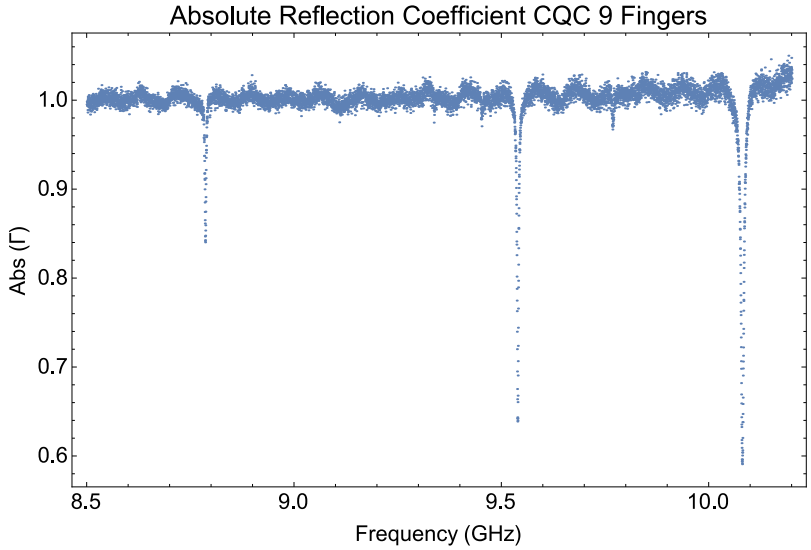

Figure 4.2: A figure showing the absolute reflection coefficient of the CQC circuit with the second lowest shunt capacitance C_i, consisting of 9 fingers. The circuit exhibits a spectrum which we cannot reproduce, with anywhere up to 6 resonances and a final resonance with by far the largest amplitude.

explanation for this phenomenon. One might be able to find a physical reason to exclude the very small resonances, but even then our model never produces a spectrum where the third resonance is by far the dominant one. Further investigation would be required to solve these issue. The other four circuits all exhibited three resonances, much like the circuits on the CQJ sample.

In the CQC samples we vary C_i as a function of shunt capacitor fingers, the dominant influence of which should be on $\omega_{1,3}$ and $\omega_{2,4}$. As in the previous section we obtain these parameter values through a joint fit together with C_{J_i}, using the values of ω_i and J_{NN} from the combined dataset of the CQJ and CQC samples. As shown in figures 4.3 (a) and (b), we

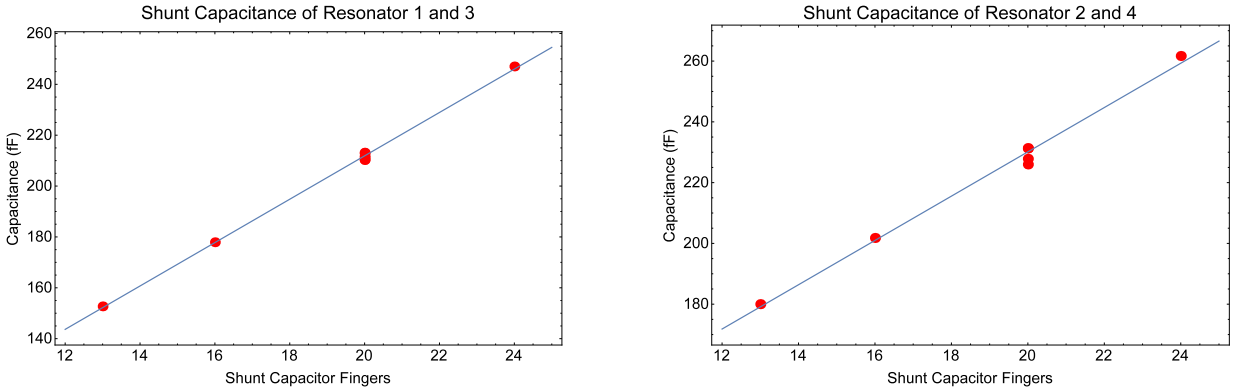

(a) *(b)*

Figure 4.3: The fitted linear relationship between the number of shunt capacitance fingers and the shunt capacitance C_i. Panel (a) shows this relationship for $C_{1,3}$ and (b) for $C_{2,4}$.

again find the expected linear dependence. The relationships are $C_{1,3} = 41.3 + 8.53 \times \#fingers$ and $C_{2,4} = 84.4 + 7.29 \times \#fingers$ in units of fF. The fact that the two linear relationships differ substantially is consistent with the fabrication mismatch between horizontal and vertical. However, one would expect to see this difference in the slope, while the main difference between the two is found in the linear offsets. In order to investigate this mismatch one could fabricate a new set of samples with less asymmetry, to verify how the offsets behave in the case of identical slopes.

4.1.3 CQK

In the sample denoted by CQK we study the variation of the capacitor coupling the resonator to the transmission line, C_κ. This is done by varying the ratio of coupling finger length to shunt capacitor finger length. In this case even less datasets could be fit: out of the six available samples, only the second and third most weakly coupled circuits were consistent with our theory, their parameter values listed in table. For the case of the most weak coupling, no resonances could be discerned at all; it is possible that they were smaller than the noise that remained after calibration, and that the system was only coupled very weakly. The three most strongly coupled resonators however showed highly irregular behaviour: as shown in Figure 4.4, they had not three, but five resonances, similar to the circuit with the lowest shunt capacitance in the previous section. However, the resonances now also have a very different shape. As of now we do not have an explanation for this. While this is not desirable, it is fortunate that this occurs at high coupling capacitances. In the experiments where these geometries will eventually be used, weak coupling is be the norm, and such effects should thus

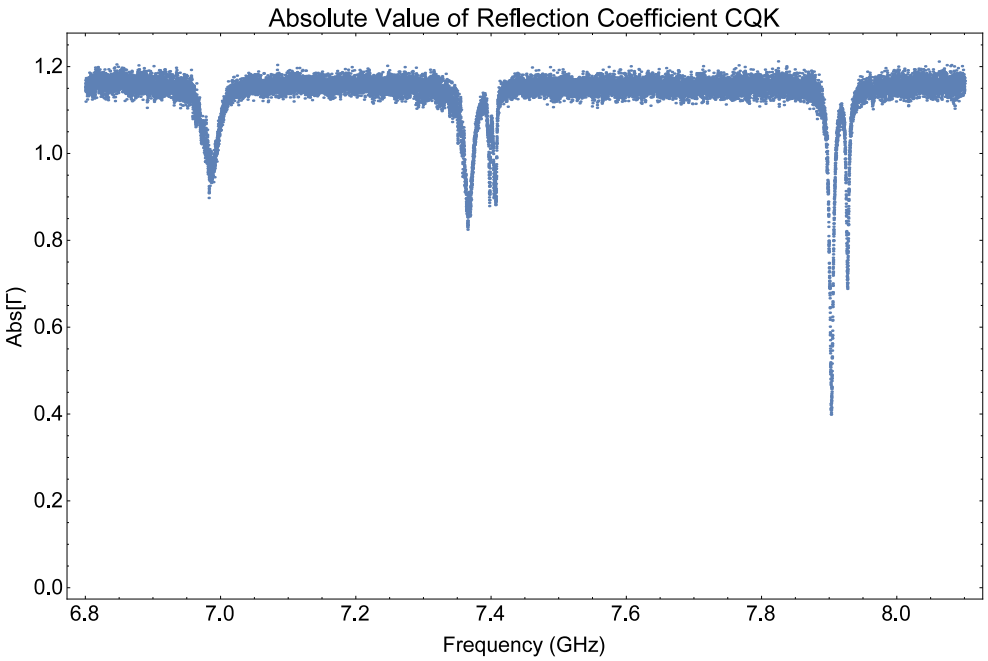

Figure 4.4: The absolute reflection coefficient of the second most strongly coupled CQK circuit, with a finger fraction of 1. While one can expect anywhere from 3 to 4 resonances with $N = 4$ resonators present in the system we observe at least 5, with anomalous shapes.

not occur. However, as only two of the circuits could be fit, the dependence of C_κ on the number of fingers can not be properly investigated as of now.

Fingers	ω_{13} (GHz)	ω_{24} (GHz)	J_{NN} (MHz)	J_{NNN} (MHz)	γ (MHz)	κ (MHz)
0.001	-	-	-	-	-	-
0.2	$2\pi \times 7.61$	$2\pi \times 7.27$	202	92.7	2.67	0.336
0.5	$2\pi \times 7.58$	$2\pi \times 7.35$	210	66.0	2.72	0.424
0.75	-	-	-	-	-	-
1	-	-	-	-	-	-
2	-	-	-	-	-	-

Table 4.3: Fitted parameters for the CQK samples. The non-integer number of fingers indicate single fingers with a fractional length as given by the values in the table. The measurements of the samples with 0.001, 0.75, 1 and 2 fingers could not be fit.

4.1.4 CQL

In sample CQL we have two circuits: one CQ circuit connected to four transmission lines, and one connected to a single one. The latter offers no new insights compared to the previous section and we thus focus on the former. The circuits studied thus far generally show 3 resonances, consistent with the picture of a diagonally pairwise symmetry. However, previously we only looked at circuits coupled at resonator 1, giving us reflection coefficient S_{11}. Here we can also study other reflection coefficients, such as S_{22} and S_{33}. Especially the comparison of the first two is interesting our scenario, as the mode that is dark should switch between the two coefficients. Moreover, for the transmission elements S_{12} and S_{21} it should be observable that both modes are dark.

While we initially expected the CQL circuit to behave in this way, this is not observed, as shown in Figure 4.5. The noise in the measurements makes it ambiguous in the respective spectra on their own, but put next to each other one can observe that $|S_{11}|$ and $|S_{22}|$ show not three but four resonances, with the dominant resonance switching from just below to just above 7.4 GHz respectively. The red dotted line serves to visually assist with recognizing this. Consistent with this is $|S_{12}$ shown in panel (c): here we see all four resonances clearly present. These findings are all consistent with a CQ system that does not have a diagonally pairwise symmetry. This in turn begs the question why we observe this in the system that is arguably most symmetric, with coupling to all four resonators. We hypothesize that the answer could lie in the design of the circuit and the chip, as shown in figure 3.2 Here one sees that while the circuit itself is symmetric, the transmission lines are not. Perhaps this is what breaks the mirror image type symmetry, giving rise to the observed measurements. However, the lines should not have too much effect, so it could also simply be that there are some discrepancies on the fabrication side. This would have to be investigated further.

It should be noted that for these measurements only 3 SMP cables were available, meaning the fourth transmission line was not connected. To take this into account, the dipstick connector connected to this fourth transmission line was terminated.

4.1.5 Comparison of the circuits

As we have now fit data from four different samples with $N = 4$ resonators, there are some statistics we can obtain. As noted before, each sample contains 1 common circuit with identical parameters. While in no way precise, this can help us determine how reliable our fitting method is through comparing the determined parameters of each of these circuits. Ideally one would obtain the exact same value every time, but in reality the parameters are distributed around a certain mean, as reported in Table 4.4. We see that

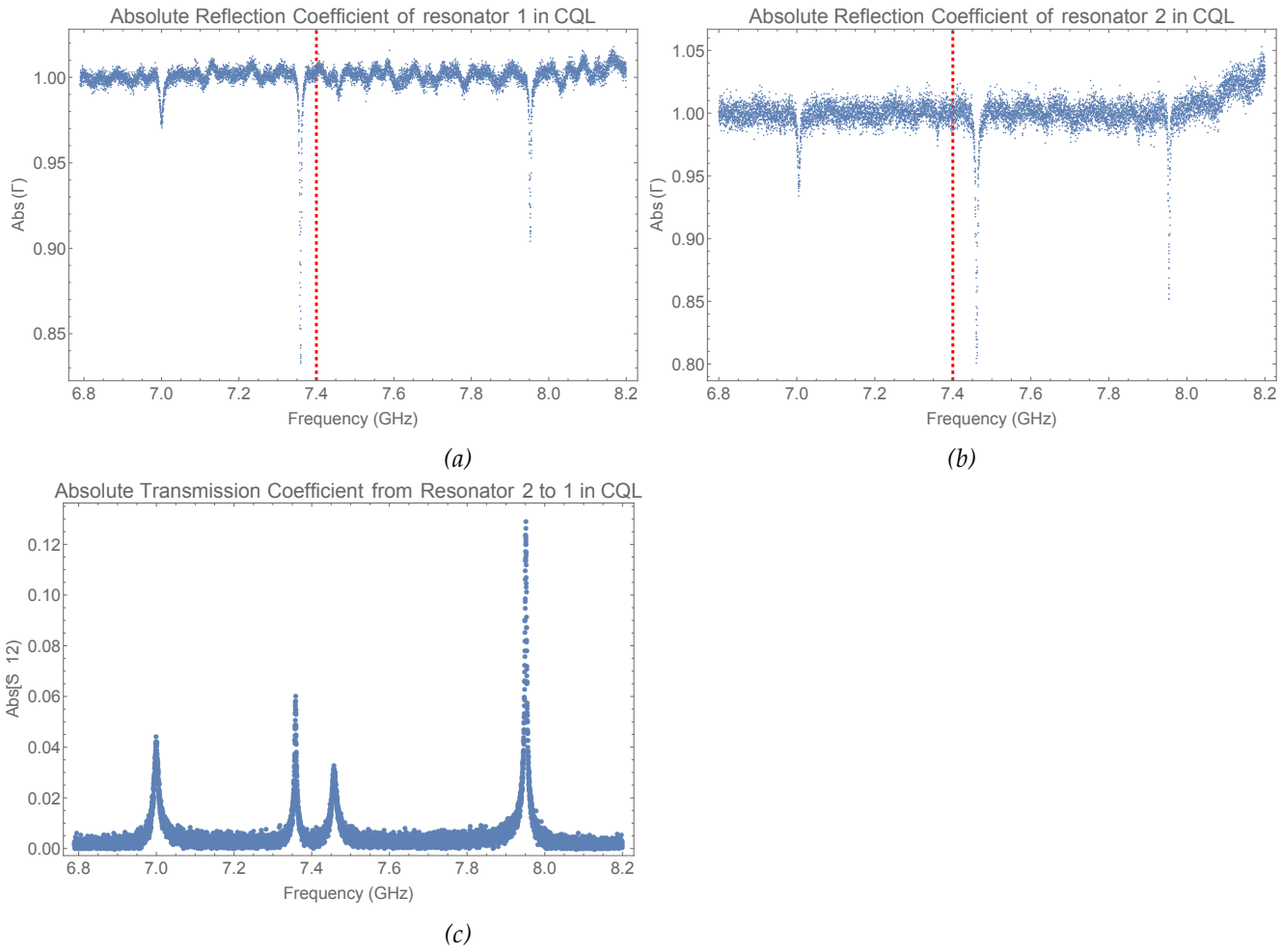

Figure 4.5: Three panels showing the absolute reflection and transmission coefficients of the CQL circuit, connected to four transmission lines. In the first panel we measure $|S_{11}|$ and detect four resonances, the fourth one hardly discernible at just above 7.4 GHz. We observe a similar spectrum for $|S_{22}|$, with one larger difference: the coupling depths of the two middle peaks have swapped. Finally, panel (c) shows $S|_{12}|$, which again shows four resonances, consistent with the above.

for ω_{13}, ω_{24} and J_{NN} the ratio of the standard deviation to the mean is very small: our fitting method appears to be consistent between measurements of identical samples. For γ and κ the ratio is already on the order of several percent, which perhaps has to do with how sensitively the fitted model depends on these parameters. Moreover it might in part be due to the fact that for κ we have neglected its weak dependence on the frequency of the input signal, and that we have taken γ_i to be equal for all i. Finally, J_{NNN} shows very large deviations, at around 20% of the mean. The exact reason for this is unclear. However, during the process of finding good initial parameters, we evaluated quite some different forms of $|\Gamma(\omega)|$, and the dependence on J_{NNN} was almost always at least a squared dependence. As this is typically a parameter that is one or more orders of magnitudes smaller than the other parameters it competes with (being ω_{13}, ω_{24} and J_{NN} as the other parameters do not enter into the Hamiltonian) it might be that its weight in the fitting method is rather small, which means that a broad range of values gives almost the exact same fit.

Parameter	Mean μ	Standard Deviation σ	$\frac{\sigma}{\mu}$
ω_{13} $(2\pi \times GHz)$	7.59	0.014	0.002
ω_{24} $(2\pi \times GHz)$	7.34	0.028	0.004
J_{NN} (MHz)	212	1.5	0.007
J_{NNN} (MHz)	72.8	15.5	0.2
γ (MHz)	2.69	0.062	0.02
κ (MHz)	0.445	0.0246	0.06

Table 4.4: A statistical comparison of the fitted parameters for the circuit that is present in each study of the circular quatromers.

4.2 Circular Trimer

On the sample of the circular trimers there are four circuits: two connected to three transmission lines (denoted by CTL), and two connected to a single line, denoted by CTJ. Each of these circuits exhibited the same type of absolute reflection resonance spectrum: three resonances, as shown in Figure 4.6a. The transmission spectrum offered no surprise here either, showing these same three resonances to be present as well (Figure 4.6b). This would be consistent with a system in which there is no reflection symmetry in the axis going through the coupled resonator, for any of the three resonators. For if any of them had this symmetry, we should have seen the presence of a dark mode in our system when coupling at different resonators in the CTL circuits. We can understand this through the way such a device is fabricated. The resonators are oriented in a type of triangle, which means the

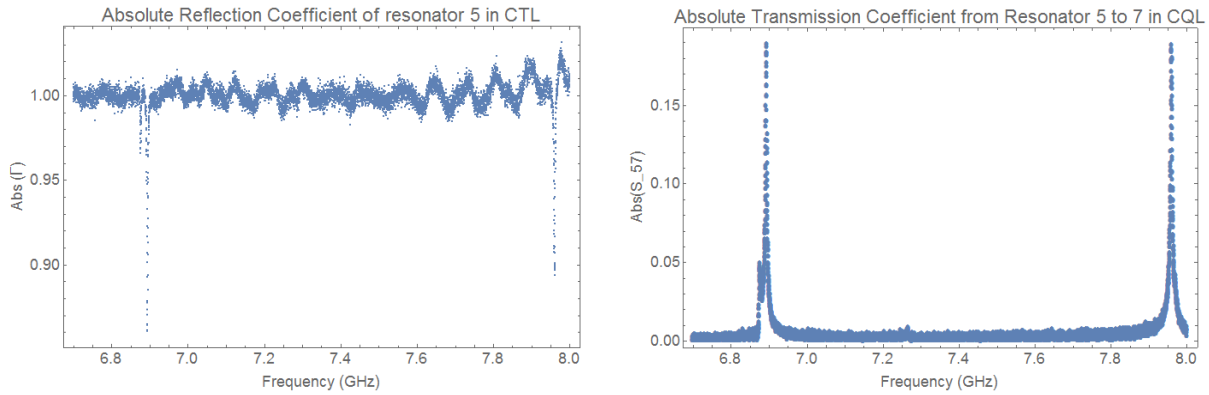

(a) *(b)*

Figure 4.6: Two panels showing the absolute reflection coefficient of a circular trimer. Both exhibiting three resonances, they indicate that the system does not have a reflection symmetry in the axis passing through the coupled resonator used to input the signal.

capacitances are at three different angles. In the CQ circuits it was found that horizontal and vertical capacitances have a discrepancy; this should in principle mean that at every angle of orientation we fabricate a different capacitance. One can therefore see the CT circuits as having three different C_i values, and thus having no symmetries other than the trivial rotational symmetry. This then implies that no modes should be dark, which is what we observe.

Applying our fitting method of the CQ system to CT posed some trouble however. If it were true that ω_i was the same for all three resonators, it should have been a straightforward process, as the model is now simpler than before. However, as we note above, the full system would in fact have three distinct ω_i, as well as a J parameter. This gives us four parameters, of which initial values have to be found based on the location of three resonances, which is an underdetermined system of equations. Finding initial parameters based on an assumption that the ω_i are approximately equal does not work either; the initial parameter values are then for a system of two resonances and not three. This leads us to conclude that in order to fit measured dynamics to a model one will either have to find a better fitting routine, or the discrepancy in fabricating conductances at different angles would have to be resolved, reducing the number of parameters in the model.

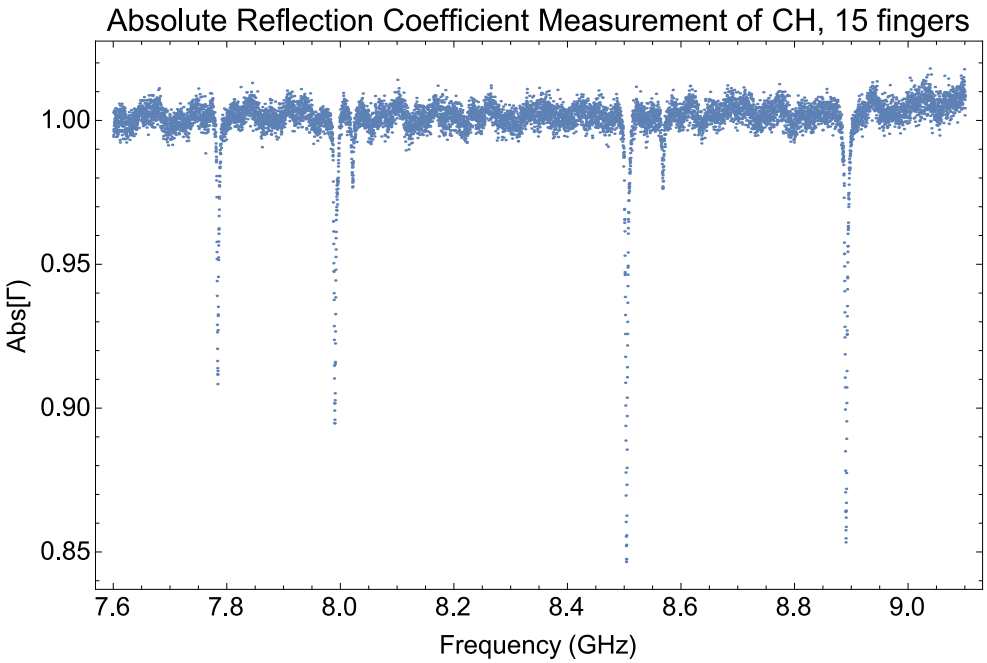

Figure 4.7: A figure showing the absolute reflection coefficient $|\Gamma(\omega)|$ of a circular hexamer of which the shunt capacitor consists of 15 fingers. Six resonances are visible.

4.3 Circular Hexamer

For the circular hexamer we study what happens under the variation of C_i; we thus study CHC. In total four circuits were available, with 10, 15, 20 and 24 fingers respectively. All four of these circuits exhibited six resonances, and the spectrum of one of these circuits is shown in Figure 4.7. This is again indicative of no reflection symmetry in the axis going through the coupled resonator. Similar to the circular trimer, the circular hexamer is a hexagonal structure with capacitances at a total of four different angles, potentially breaking the aforementioned symmetry. It is thus not expected for this system to have any dark modes, consistent with the measurements. Moreover, the problems of fitting the data encountered in the CT circuit are exacerbated here, as one now needs a total of 3 different ω_i and three orders of J terms in a model that is becoming more complicated, at it is based on a six by six Hamiltonian.

4.4 Circular Octomer

Two different types of circular octomers were fabricated: one connected to a transmission line at a single resonator, and one connected to a transmission

line at all eight resonators. As of this project, we only measured the first type. This is because it was not yet clear how to proceed with the circuit connected at eight sites. In order to find all 64 scattering matrix elements with only three cables to connect to the sample at once, a very large amount of dipstick measurements would have to be performed with numerous recalibrations. However, seeing how the dynamics from CQL generalize to this structure is certainly of interest and one should consider finding an efficient way to study this system in the future.

On the other hand, we did measure the circuits connected at a single resonator. Two different circuits were fabricated, with 3 and 5 J coupling capacitor fingers each. The resulting measurement of the first of these is shown in Figure 4.8 (a). As can be seen, at least six resonances are present. It is however hard to tell if there are not up to eight resonances, as their amplitudes might be on the order of the noise. A more accurate measurement is required to make any conclusions about this with confidence. Panel (b) serves to illustrate this with a theoretical spectrum, not obtained from a fit. Nevertheless, it is clear that there are more than five resonances, and that like the circular hexamer our system appears to not have the required reflection symmetry. One can make the same argument here, namely that now capacitors at four different angles are present in the system, breaking the mirror image symmetry. Moreover, fitting was again not successful, for the reasons listed before.

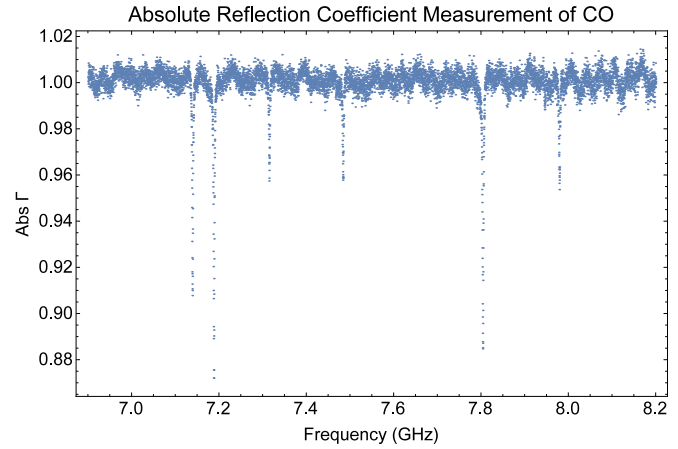

(a)

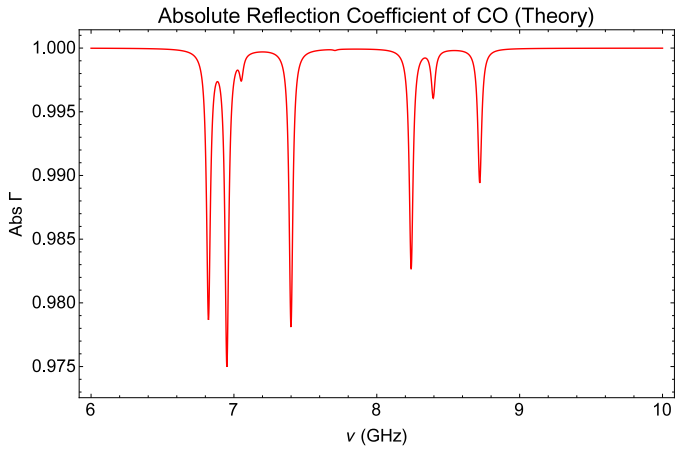

(b)

Figure 4.8: Two panels showing the absolute reflection coefficient of a circular octomer. The first panel shows the actual measurement, with at least six resonances visible. This circuit is fabricated with three coupling capacitor fingers. As the second panel serves to illustrate however, more resonances could be obscured by the noise. The second panel shows a theoretical spectrum for such a circular octomer, where we chose C_i values in pairs based on their fabrication angle. Not visible at this scale is the eight resonance around 7.8 GHz, with an amplitude over 50 times smaller than the deepest resonance. Important to note is that this spectrum is not obtained from a fit, it merely depicts how big the differences in relative amplitudes can be between the resonances and thus that it is difficult to make a definite statement based on relatively noisy measurements.

Chapter 5

Conclusion and Outlook

In this thesis we studied the scattering matrix elements of coupled RLC resonators with periodic boundary conditions. We began by analysing the physics of the system, using the Lagrange, Hamilton second quantization and input output formalisms. What we found were matrix elements not unlike the case of a linear chain of resonators, with one major difference: the occurrence of dark modes. Subsequent investigation into the eigenvectors of the Hamiltonian as well as the symmetries of regular polygons revealed that these dark modes required a distinct symmetry of the system. Only if the system has a reflection symmetry in the axis through the coupled resonator do the dark modes occur; it appears that traversing the circuit clockwise or anticlockwise should be indistinguishable. If this is the case, several components of the eigenvectors will be zero. As the eigenvectors of a Hamiltonian are directly linked to the eigenstates of the system, these zero components denote probability densities, and thus predict the absence of the field at these sites. While a future formal derivation might be desirable, this led us to make a link to systems exhibiting (destructive) interference. Investigation of the dispersion relations of these circuits provides insight into the amount of resonances we expect for a circuit of N resonators that has the required reflection symmetry: $\frac{N}{2}+1$ for even N, and $\frac{N}{2}+\frac{1}{2}$ for odd N. This in turn tells us that if we detect more resonances, the required symmetry is not present.

We then discussed the experimental aspects of the research, beginning with a description of the physical devices. The circuits (not fabricated as part of this thesis) consist of structures written in a niobium layer deposited on top of a sapphire substrate, containing inter-digital capacitors and meander inductors. As the circuits were connected to one or more transmission lines via a coupling capacitor, we were able to perform measurements of the scattering matrix elements of various circular geometries. These ranged from the circular trimer ($N = 3$ all the way to the circular octomer ($N = 8$). The

measurements themselves were performed with a dipstick, liquid helium dewars, and a vector network analyser (VNA) connected to the dipstick using SMP cables. Reflection coefficients were obtained for all circuits, as well as transmission coefficients for the circuits connected to more than a single transmission line. Subsequently a fitting method was developed, incorporating the possibility of dark modes as well as the unfortunate mismatch between capacitances fabricated at different angles. In this thesis only the absolute value of the reflection coefficients were fit; future endeavours could investigate the inclusion of other data (such as the angle and the real and imaginary parts) as well in order to obtain more reliable fitting data.

Most of the analysis was performed for four different CQ circuits: CQJ, CQC, CQK and CQL, which varied the coupling capacitance C_{Ji}, the shunt capacitance C_i, the coupling capacitance C_κ and the number of transmission lines respectively. The study of C_{Ji} turned out to be the most accommodating; all circuits exhibited three resonances and the fitting routine converged for each of them. However, the exact relationship between J_{NN} (which we extract from the data) and C_{Ji} is rather complex, so we utilized a joint fitting method to obtain values of C_{Ji} and C_i simultaneously from both J_{NN} and ω_i. The linear relationship $C_{Ji} = 1.05 + 4.35 \times \#fingers$ in units of fF was found.

The CQC circuits were mostly well behaved too, with four out of six circuits showing the same type of spectra as the CQJ circuits. However, the two circuits with the lowest shunt capacitance values exhibited highly unexpected behaviour, exhibiting as many as six resonances in a 4 resonator system. No explanation from theory could be given, nor was an explanation found on the basis of experimental considerations. This is therefore an issue that should be further investigated moving forward. However, using only the four well behaved circuits, a linear relationship was also found between the number of shunt capacitance fingers and the resulting capacitance C_i, again based on a joint fitting method. The relationships that were found are $C_{1,3} = 41.3 + 8.53 \times \#fingers$ and $C_{2,4} = 84.4 + 7.29 \times \#fingers$ in units of fF. While asymmetry between horizontal and vertical was expected, the large difference in linear offset was not and should also be investigated further.

The pattern of odd resonance spectra continued in the CQK samples, where only 2 out of 6 circuits behaved as expected. The most weakly coupled circuit appeared to not exhibit any coupling at all, while the three most strongly coupled systems showed highly irregular resonance spectra with odd lineshapes and more than 4 resonances. In this study no linear relationship could be found between C_κ and the number of fingers, due to the small sample size. We suggest to perform a subsequent investigation of parameter dependence on C_κ, but instead for a range of lower couplings than the majority of the ones investigated here. This is because they seem to produce more well behaved spectra, and future applications of the circuits will most

likely require weak coupling.

The CQL circuit, coupled to not one but four transmission lines, marked a departure from the dark modes seen in the other CQ circuits. Exhibiting all four resonances in every case, we had a strong indication that the system did not have the required reflection symmetry expected from a fabricational point of view. We theorize that perhaps the asymmetry of the fabricated transmission lines could be the cause of this symmetry breaking, or that it could simply be caused due to errors in the fabrication of the circuits themselves. Future endeavours should also explore connecting the ground planes via wirebonds, to suppress chip modes which could introduce cross couplings or similar phenomena.

Like the CQL circuits, the CT, CH and CO systems with $N = 3, 6, 8$ resonators respectively also did not have any dark modes, again informing us of a lack of reflection symmetry in the axis through the coupled resonator. Here however the cause seemed more apparent; as it was found that during fabrication the capacitance constructed has an angular dependency, one would not expect these systems to have this symmetry to begin with. This however posed a problem for fitting the measured spectra. The angular dependence of the capacitances meant that one could not assume each resonator to have the same resonance frequency ω_i, quickly increasing the number of parameters of the model. This greatly complicated the process of finding good initial parameter values, and in the end led to us not being able to fit any other data than for the circular quatromers, the only system exhibiting the dark modes. Improvement is definitely needed in this area, but can be readily achieved by solving the angular dependence of capacitance fabrication. This would lead to a strong reduction in the number of different parameters in the system, leading to a larger degree of symmetry and simpler fitting models.

All together, most of the measured systems behaved in accordance with how one would expect them to from theory. For the systems with enough symmetry dark modes were observed. While a formal understanding of the occurrence of the dark modes was not formed, one can question its usefulness for future endeavours as these linear circuits are but a stepping stone to more complicated, non linear systems. For the CQ circuits fitting parameters was possible and often even very precise based on visual confirmation of the fits, and dependencies were extracted. Improvement is still required here however, as error estimates are not available in the current procedure, and both γ and κ fits appear to be unreliable. While the method developed for fitting CQ systems should be generalizable to other geometries, their subsequent data fitting was not possible due to the aforementioned fabricational angular dependence of capacitances. Future endeavours should probably aim to either understand the exact dependence or get rid of it all together, poten-

tially allowing one to extract relevant parameters from all studied systems as well as inducing the more exotic dark mode physics.

Appendix A

Visualizing Eigenvectors of Systems with Periodic Boundary Conditions

The circuits studied in this thesis all have one common property, being that they are coupled in a circular fashion. In chapter 2, rather extensive analysis of the eigenvectors of the Hamiltonian of these systems is performed in a numerical fashion, which is greatly simplified through a clear visual representation of said vectors. Based on a concept for eigenvector plotting in a linear array, we explored several options of plotting these eigenvectors in a simple, transparent fashion that allows the user to quickly read off magnitudes and sign differences while also stressing the periodicity.

In order to present the various alternatives explored in the simplest way possible, we first look at the various alternatives for $N = 4$, the circular quatromer. We choose our parameters to reflect the diagonally pairwise symmetric case from chapter 2, with $C_{1,3} = 0.9C_{2,4}$. In order to reduce the amount of clutter we omit a figure caption, and simply discuss the different figures here. After discussing $N = 4$ we also take a look at $N = 8$ (circular octomer) in order to see how the clarity of the figures varies with system size.

Before we discuss the differences, we first note the factors common to all figures. For system size N, each figure has N objects i for the N different eigenvectors, ordered from left to right in order of increasing eigenvalue. Each object i then again has N components, denoting the different elements of the eigenvector. In the linear case the front object denotes element 1 and the back object element N, while in the case of circular geometries the ordering is based on the unit circle in the x-y plane. The first element of the eigenvector is represented by the first object in the positive section of the x-y plane, while the Nth element is represented by the last object in the negative y, positive x plane. The color red denotes that the vector element is positive, while the color blue denotes negative. In the case of the 3D

figures height denotes the relative magnitude of the vector elements, while the direction in which the figure is drawn from the $z = 0$ plane denotes the sign; upwards for positive and downwards for negative. For the 2D figure no such directionality is imposed and the sign is only denoted by color. Moreover, the relative magnitude of each vector element is denoted not by the radius but by the area of the circular segment.

Figure A.1 shows the visualization with which we began, inspired by previous work on linear arrays. The relative magnitudes and sign differences are apparent here, and the mode structure is clearly visible. However, periodicity is not included in any way and one thus has to impose these conditions in their own mind in order to relate what is being shown the the physical system. Figure A.2 offers improvement in this area, as the cuboids are now placed on a circle. Here it is clear that in the second eigenvector two diagonally opposing resonators have nonzero components, as expected from the choice of parameters. For $N = 4$ it is still relatively easy to visually distinguish each component as not too much overlap is taking place. Figure A.3 shows a variant of this, where the cuboids are now replaced with cylinders. This adds an extra flavor of periodicity to the structure. Figure A.4 takes this one step further. Instead of drawing a separate cylinder for each resonator, they are now all combined into a single object, with each element represented by a cylindrical wedge. This offers the aesthetic advantage of showing clearly which resonators are connected to each other, while slightly obfuscating some components due to overlapping graphics. Finally, figure A.5 shows a two dimensional variant of the above: the cylindrical wedges are now replaced by circular segments. The obvious downside of this is that sign differences are now represented only by color, requiring the viewer to take an extra step in order to understand the figure. However, this approach provides very clear visuals as none of the components can overlap, possibly making other segments less clear.

While some of the figures might be more visually pleasing than others, most of them seem to work well for $N = 4$. For $N = 8$ we choose a completely symmetric system, where all resonators have the same parameter values. Figures A.6-A.8 remain relatively clear, although quite full, with some overlapping visuals. Especially discerning relative height differences between different components is difficult. One could think about how to implement a better color coding scheme, where perhaps the colors scale from blue to red when the eigenvalues go from -1 to 1 respectively. Figure A.9 illustrates that a single cylinder is simply too little space to represent eight different sections. Some parts are overlapping, and the mode structure is not always obvious. Figure A.10 again shows that, although the distinction between positive and negative is less obvious, the two dimensional representation provides an unambiguous and quick way to analyse the eigenvectors. We choose to use this way of representing the eigenvectors in the thesis.

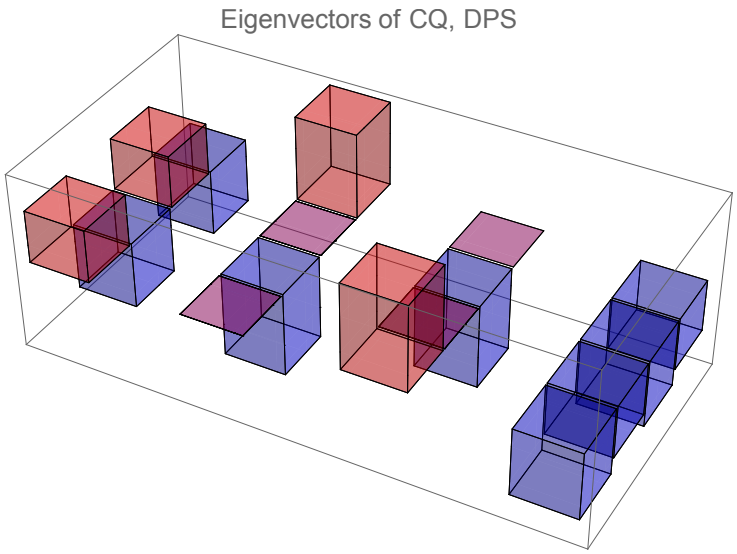

Figure A.1

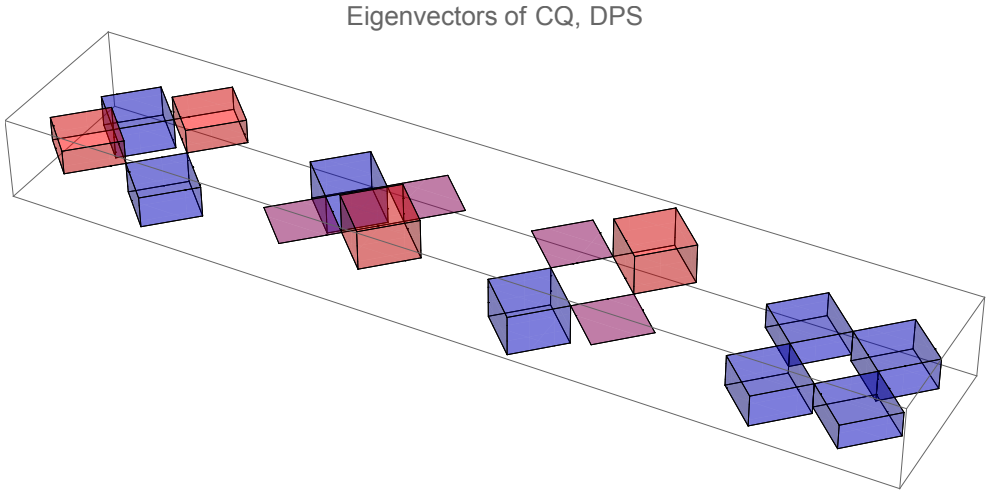

Figure A.2

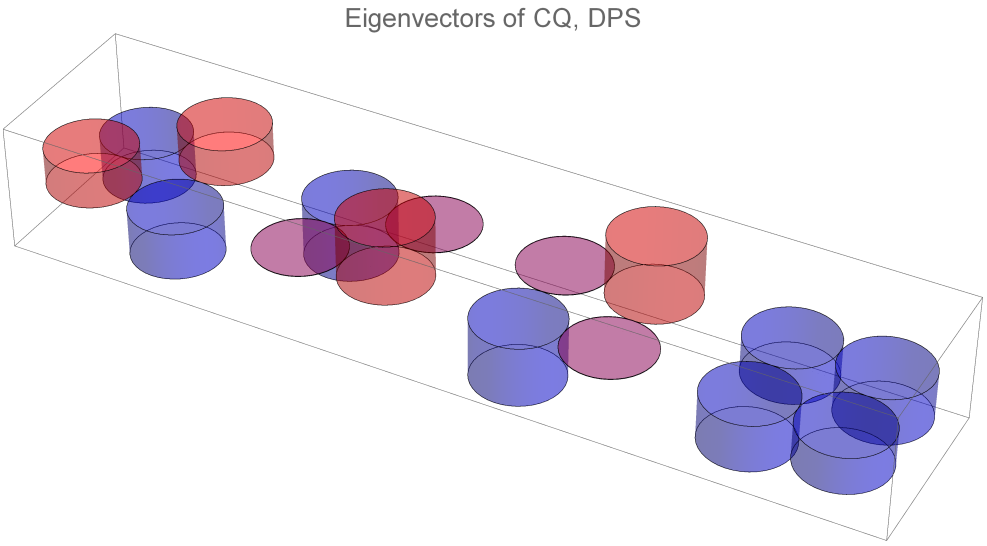

Figure A.3

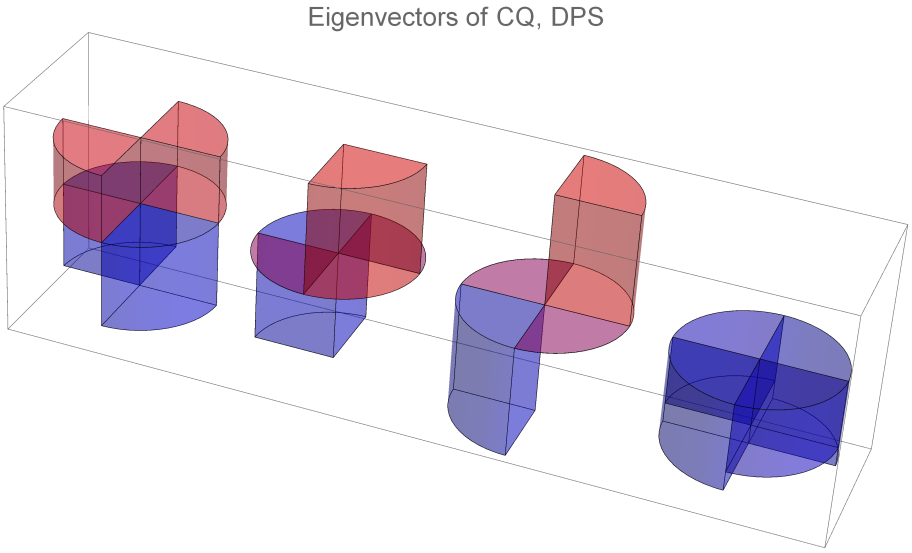

Figure A.4

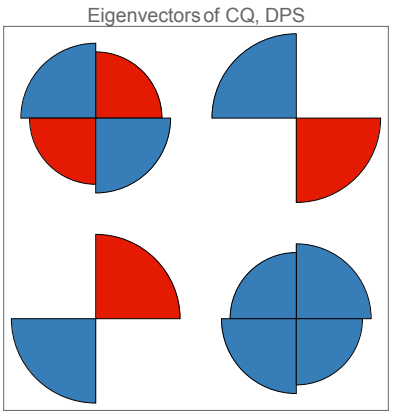

Figure A.5

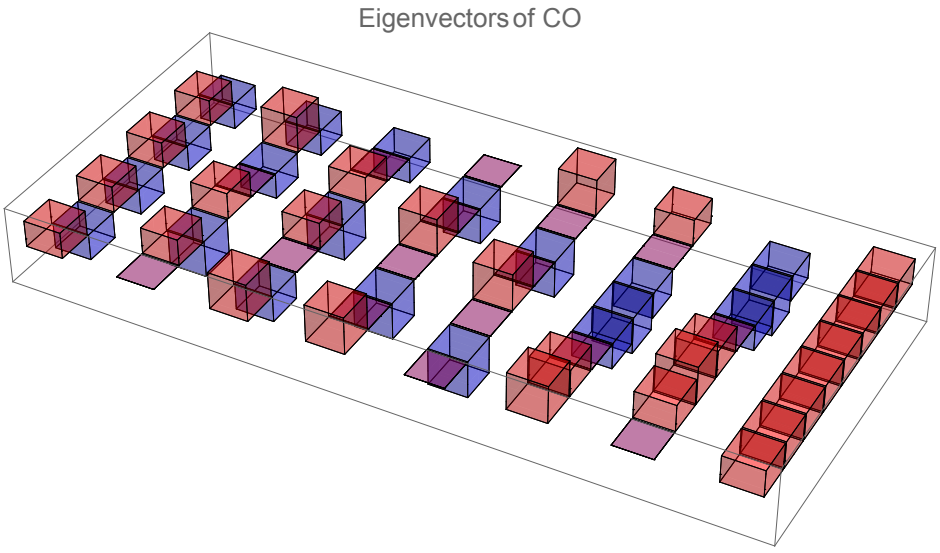

Figure A.6

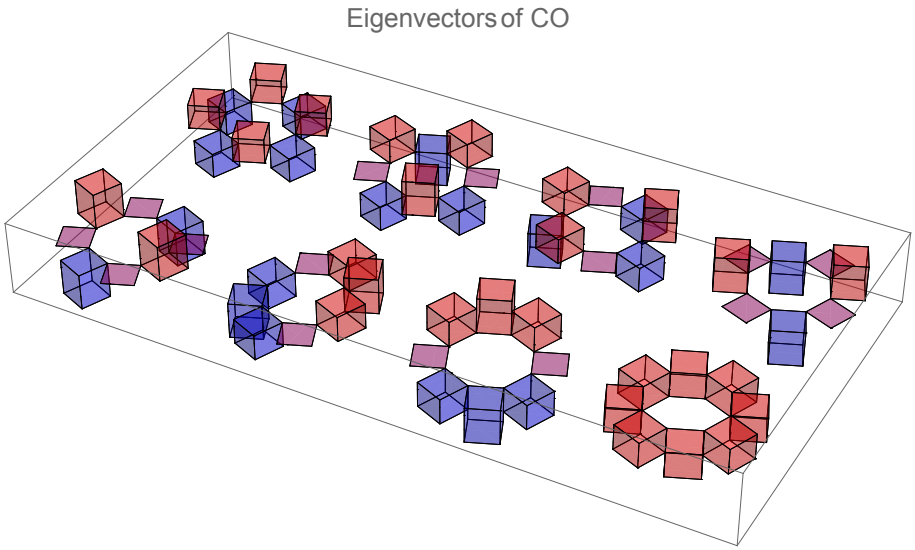

Figure A.7

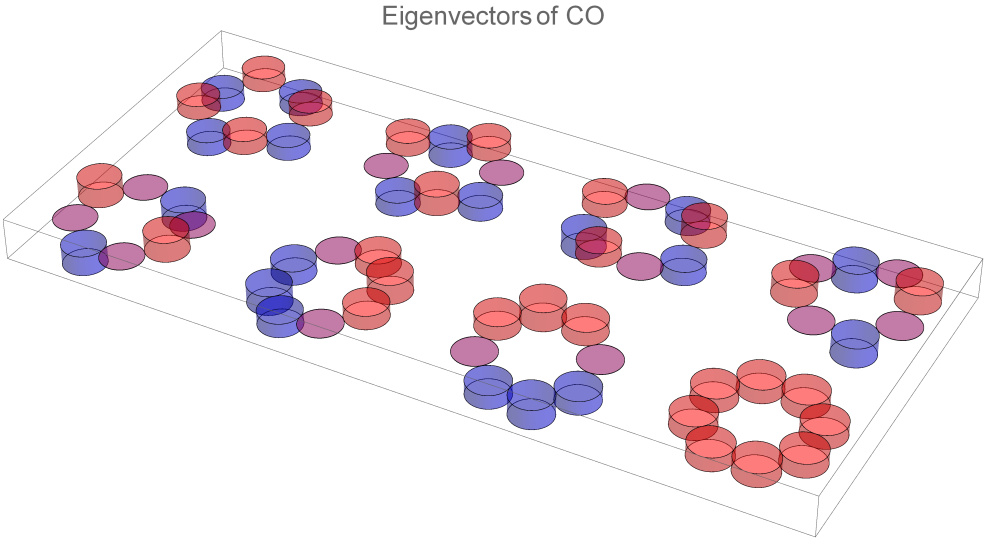

Figure A.8

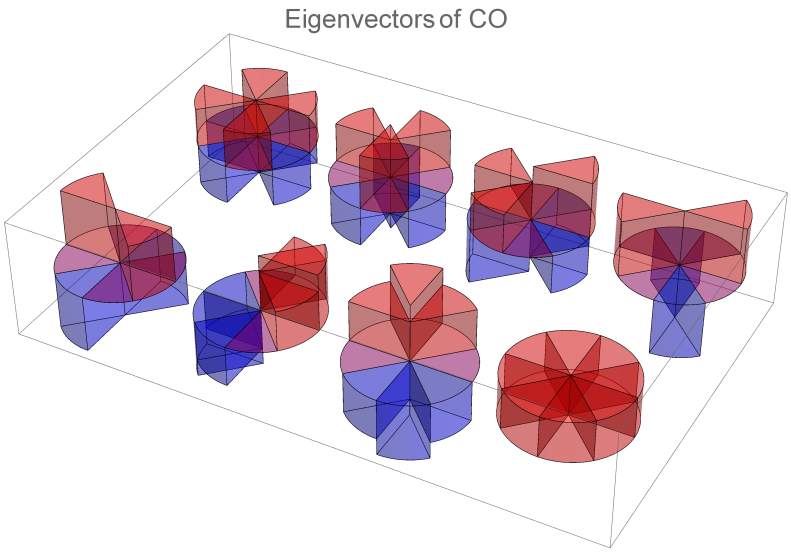

Figure A.9

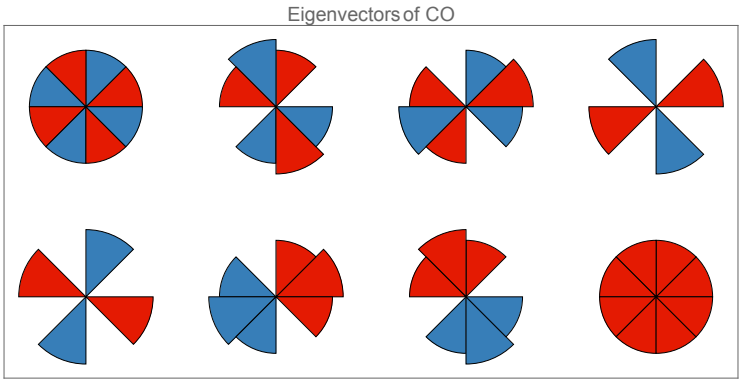

Figure A.10

Bibliography

[1] Antonio Rubio Abadal, *Josephson Parametric Amplifiers with Lumped-element Coupled Resonators*. Master Thesis, ETH Zürich, Apr. 2015.

[2] M. A. Nielsen and I. L. Chuang, *Quantum Computation and Quantum Information*. Cambridge ; New York: Cambridge University Press, 1 ed., 2000.

[3] I. Georgescu, S. Ashhab, and F. Nori, "Quantum simulation," *Reviews of Modern Physics*, vol. 86, pp. 153–185, Mar. 2014.

[4] P. Nalbach and M. Thorwart, "Enhanced quantum efficiency of light-harvesting in a biomolecular quantum "steam engine"," *Proceedings of the National Academy of Sciences*, vol. 110, pp. 2693–2694, Feb. 2013.

[5] G. S. Engel, T. R. Calhoun, E. L. Read, T.-K. Ahn, T. Mančal, Y.-C. Cheng, R. E. Blankenship, and G. R. Fleming, "Evidence for wavelike energy transfer through quantum coherence in photosynthetic systems," *Nature*, vol. 446, pp. 782–786, Apr. 2007.

[6] E. Harel and G. S. Engel, "Quantum coherence spectroscopy reveals complex dynamics in bacterial light-harvesting complex 2 (LH2)," *Proceedings of the National Academy of Sciences*, vol. 109, pp. 706–711, Jan. 2012.

[7] D. C. Giancoli, *Physics for Scientists and Engineers with Modern Physics*. Upper Saddle River, N.J.: Pearson Prentice Hall, 2008.

[8] A. Potocnik, *Towards Input-Output Theory for an Array of Coupled Lumped-Element Resonators*. Unpublished Internal Document, ETH Zürich, 2015.

[9] C. Cohen-Tannoudji, J. Dupont-Roc, and G. Grynberg, *Photons and Atoms: Introduction to Quantum Electrodynamics*. Physics textbook, Weinheim: Wiley, nachdr. ed., 2004.

[10] D. S. Dummit and R. M. Foote, *Abstract Algebra*. Hoboken, NJ: Wiley, 3rd ed ed., 2004.

[11] D. J. Griffiths, *Introduction to Quantum Mechanics*. Upper Saddle River, NJ: Pearson Prentice Hall, 2nd ed ed., 2005.

[12] N. W. Ashcroft and N. D. Mermin, *Solid State Physics*. New York: Holt, Rinehart and Winston, 1976.

[13] "Discrete Fourier Transforms - Wolfram Language Documentation," 2015.

Eidgenössische Technische Hochschule Zürich
Swiss Federal Institute of Technology Zurich

Declaration of originality

The signed declaration of originality is a component of every semester paper, Bachelor's thesis, Master's thesis and any other degree paper undertaken during the course of studies, including the respective electronic versions.

Lecturers may also require a declaration of originality for other written papers compiled for their courses.

I hereby confirm that I am the sole author of the written work here enclosed and that I have compiled it in my own words. Parts excepted are corrections of form and content by the supervisor.

Title of work (in block letters):

Coupled Lumped-element Resonators with Periodic Boundary Conditions

Authored by (in block letters):
For papers written by groups the names of all authors are required.

Name(s):	**First name(s):**
Bargerbos	Arno

With my signature I confirm that

- I have committed none of the forms of plagiarism described in the 'Citation etiquette' information sheet.
- I have documented all methods, data and processes truthfully.
- I have not manipulated any data.
- I have mentioned all persons who were significant facilitators of the work.

I am aware that the work may be screened electronically for plagiarism.

Place, date	**Signature(s)**
Zürich, 03-07-2015	Arno Bargerbos

For papers written by groups the names of all authors are required. Their signatures collectively guarantee the entire content of the written paper.